MSc Thesis

Controlled spherulitic crystal growth from salt mixtures

T.J. Heeremans

Under guidance of Prof. dr. N.F. Shahidzadeh
Soft Matter Group, Institute of Physics, UvA

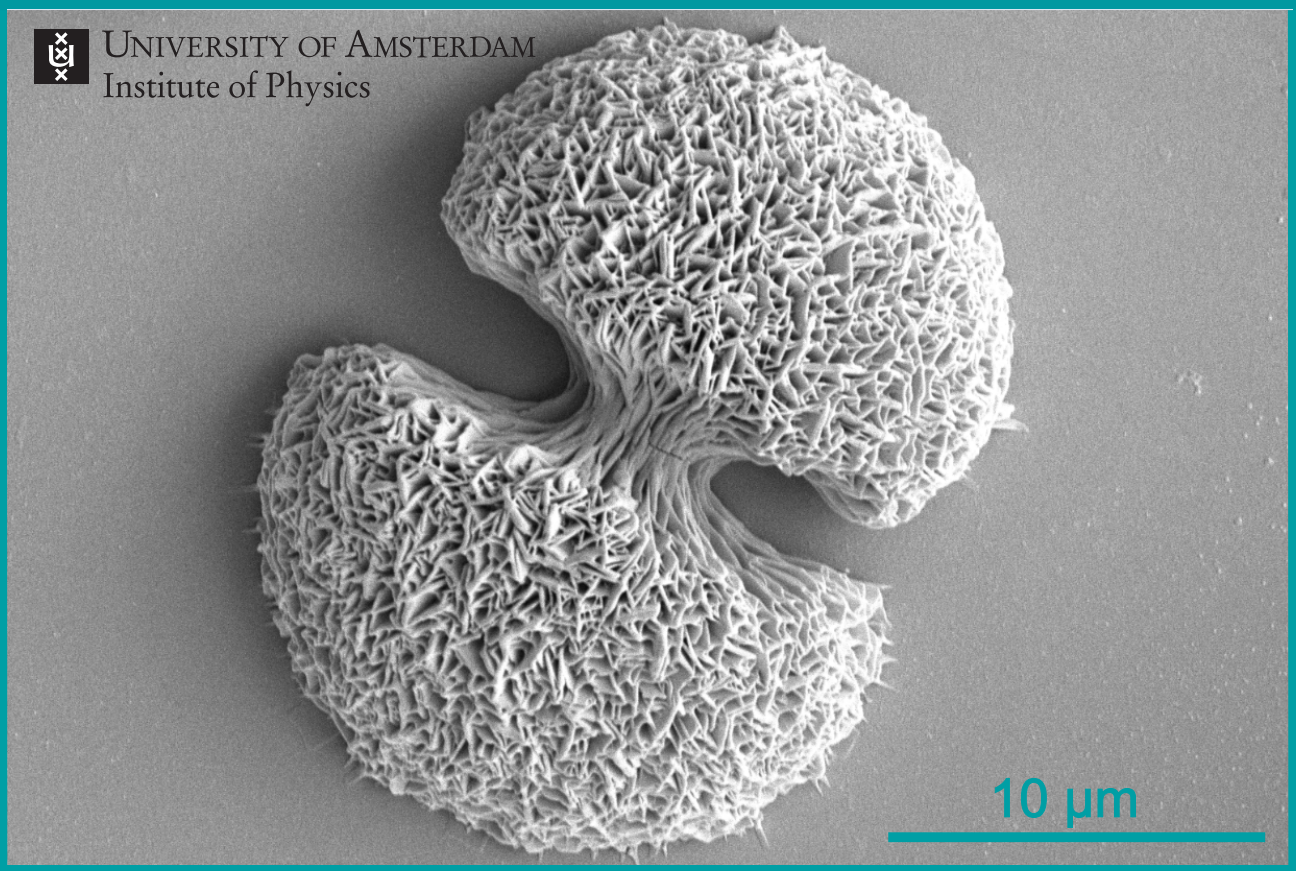

TU Delft

Controlled spherulitic crystal growth from salt mixtures

by

T.J. Heeremans

Abstract

For the first time, we present data on the actual growth rate, supersaturation, viscosity, and growth mechanism that lead to spherulitic growth. So far, fundamental questions regarding the growth conditions, mechanisms, and the necessity of a viscous growth medium have remained unresolved. Surprisingly, we observed a sol-gel transition in evaporating silica-free sulfate mixtures, followed by the growth of sodium sulfate spherulites. We characterized the spherulites' morphological evolution and chemical/structural composition using various microscopy techniques and Raman Spectroscopy. The study reveals that faceted crystals, during their morphological evolution, can transiently exhibit a spherulitic morphology before attaining their final shape. We demonstrate that adding bivalent ions to sulfate solutions can create the conditions required for the spherulitic growth of the crystal phase. We show how to obtain perfectly developed spherulites through an in-depth experimental investigation of ion concentrations, evaporation rate, and geometric constraints. Moreover, quantifying the growth conditions enables a precise understanding and facilitates a comprehensive discussion on a general approach for cultivating spherulites through solvent evaporation that is imperative for innovative purposes.

to obtain the degree of Master of Science
at the Delft University of Technology,
to be defended publicly on Monday January 29, 2024 at 10:00 AM.

Student number:	5644658	
Project duration:	March 29, 2023 – January 29, 2024	
Thesis committee:	Prof. dr. N. F. (Noushine) Shahidzadeh,	UvA, supervisor
	Dr. P. (Poulumi) Dey	TU Delft, MSE supervisor
	Dr. H. B. Eral	TU Delft

This thesis is confidential and cannot be made public until January 24, 2026.

An electronic version of this thesis is available at `http://repository.tudelft.nl/`.

TU Delft

Foremost, I extend my gratitude to Prof. Dr. N. F. (Noushine) Shahidzadeh, who allowed me to conduct my master's thesis on this fascinating topic within her group at the UvA. Your creative approach to science is inspiring and has taught me so much. And as a woman in science, I look up to your extraordinary achievements. Furthermore, a special thanks to my MSE supervisor, Dr. Poulumi Dey. Although you were not supervising the content of the research, your advice and our regular meetings helped me so much in the process. Moreover, I have greatly appreciated your patience and great approach to teaching during the master's program in Materials Science & Engineering. Also, a big thanks to Dhr. H.B. Eral, for joining my defence committee. Unfortunately, we did not collaborate on this project, but I hope we will cross paths again in the future! And I hope you will enjoy the research presented in this thesis.

Secondly, I would like to acknowledge that this master thesis is part of a research project, which is a collaboration between many esteemed researchers: Simon Lepinay, who performed the Raman Spectroscopy experiments, and I worked closely together on this project. Thank you for all the help with the experiments and our great discussions. I very much enjoyed our coffees and walks outside :). I express my gratitude to R. Le Dizès Castell, the gel expert, for your active involvement and valuable assistance in both experimental work and the interpretation of gel experiments. Without your expertise, the project would not have advanced as seamlessly. Special recognition goes to I. Yusuf, whose outstanding results in his bachelor thesis ignited the initial spark for this project. His foundational work laid the groundwork for the subsequent research, and I am truly grateful for his contributions. I would like to acknowledge P. Kolpakov for his instrumental role in conducting rheological measurements. His expertise and assistance in the lab significantly enhanced the quality of our project. R. Wijnhorst, thank you for your valuable support in the capillary experiments. I appreciate your dedication and input, which enriched our understanding of the experimental outcomes. I extend my thanks to M. Steiger for providing essential solubility data of the sulfate salt mixtures. This data played a pivotal role in the interpretation of our experimental findings. Furthermore, I express my gratitude to the skilled technical assistance provided by the workshop of the University of Amsterdam. Their proficiency greatly contributed to the success of our experiments.

Furthermore, working with others in the research group has been invaluable. I want to thank again Paul, Romane, Simon, and Rozeline for teaching me new lab skills and consistently supporting me with their intelligence and kindness. In times of scientific or personal challenges, I have always felt tremendously supported by you. Also, to the others in the Soft Matter Group, thank you for your kind advices, you are all so great, and I am going to miss working together with you! Moreover, I want to thank my UvA bachelor thesis supervisors, Prof. dr. Daniel Bonn, Prof. dr. Sander Woutersen, and Dr. Antoine Deblais. I am truly thankful for the invaluable advice you have generously shared with me throughout the years. Antoine, your exceptional supervision has equipped me with the skills and confidence to tackle any subsequent project. Many times during my master's thesis, I found myself contemplating what approach you would take when facing a difficulty. From MSE, I would also like to thank Dr Ir. J.G. Vogtländer and Prof. Dr. Ir. J. (Jilt) Sietsma, for their mentorship, which greatly influenced my studies and career. Moreover, I thank technicians Remko Seijffers and Jurriaan van Slingerland. I will leave Delft with great memories of the days I spent in the welding workshop. Last but not least, I want to express my appreciation to Bart, Isis, Britt, Alice and my mother Wendela for their tremendous support in life, allowing me to focus on this project. Thank you for your support Mila and my sister Jocelyn, who were also writing their theses, we did it! I can only hope that the quality of my thesis matches the high standards set by both of yours. Also to all my other friends and family, I love you and I can't wait to spend more time together!

T.J. Heeremans
Amsterdam, 16-1-2024

Contents

1 Introduction

1.1. Introduction

Spherulites are polycrystalline structures that are formed through magnificent self-assembly of aggregated tiny crystals that originate from a centre point and align radially outwards [28]. This morphology results from crystal growth in a radial splay accompanied by non-crystallographic branching. The occurrence of spherulites is a well-established phenomenon observed in a wide range of materials, including polymers, glasses, minerals, metals, and organic materials that are comprehensively listed in the review of Shtukenberg et al. [65]. In the medical field, spherulites are associated with kidney stone formation and amyloid disorders such as Parkinson's disease and Alzheimer's disease [67, 5, 39], while mineralogists are studying meters wide mega spherulites in rhyolitic lava [11]. The first scientific reports mentioning spherulites date back to 1837 [74]. However, interest really flourished at first in the polymer industry [48, 7, 78]. Nowadays, it is clear that spherulites can have many exciting applications because of their spherical shape and high volume-to-surface ratio. For example, spherulites are reported to increase the flowability compared to flaky crystals [44]. Moreover, they have gained interest in the pharmaceutical industry to improve drug solubility and the efficiency of PV cells [2, 45]. Unfortunately, the case-by-case studies that are reported so far do not allow for a general understanding of spherulitic growth. Moreover, the mathematical approach of simulations on nucleation and spherulitic growth limits translation to parameters that can be tuned in practice. However, harnessing the potential of spherulites in these innovative applications necessitates a profound understanding of how to control their growth since morphological features of a crystal arise from its growth history [73].

The growth rate of crystalline structures can be governed by the kinetics of incorporation of atoms on the crystal surface or by the rate at which the atoms travel towards the surface by diffusion. An adapted Damköhler number can be used to determine which of the two is the limited factor that describes the timescale of interest. The definition of the Damköhler number is given by $Da = \frac{G}{D}$, where D is the diffusion rate, and G is the integration rate. If $\mathrm{Da} \gg 1$, the integration rate is much greater than the diffusion rate distribution, the timescale is diffusion-limited. For $\mathrm{Da} \ll 1$ diffusion occurs much faster than the reactions at the surface, thus the integration rate is important to describe the time scale of interest. When the growth is surface-limited, the crystal grows linearly in time ($L \propto t$) while if the growth is limited by diffusion the growth is proportional to the square root in time ($L \propto \sqrt{t}$). The growth mechanism may often transition from integration-controlled to diffusive-controlled as the conditions change. A high driving force (high supersaturation or undercooling) tends to favour diffusive-controlled growth due to the increased kinetic factors, forming smaller, finer structures. On the other hand, lower driving forces are more conducive to integration-controlled growth, promoting the development of larger crystals with distinct facets. In his book *'Crystals: Growth, Morphology, and Perfection'* Sunagawa spherulites describes how spherulites appear at high driving force, just as dendritic and fractal growth [71]. However, a quantitative description becomes imperative to understand under which conditions spherulites are formed in nature and, simultaneously, for devising processes that can deliberately induce spherulitic growth for innovative applications.

Other theories attempting to elucidate spherulitic growth predominantly revolve around explaining the non-crystallographic branching of spherulites. They are derived from a diffusive model of constitutional

cooling broadened through the lens of the Mullins-Sekerka instability, which is also used to explain dendritic growth [34, 51, 25, 41]. This model is subsequently expanded to incorporate a hydrodynamic scaling factor to account for the radial splay [77]. Although compelling evidence strongly supports the diffusion-limited control mechanism in spherulitic growth, achieving unanimous agreement remains elusive [31, 65]. More recent studies argue that different growth mechanisms govern distinct phases during the spherulitic growth [66, 88]. A more widely acknowledged phenomenon is that spherulites develop in viscous fluids, as observed by Magill, who concludes that the physical explanation for the growth of spherulites lies in a critically large viscosity [16, 48]. Shtukenberg et al. argue, on the contrary, that viscous growth media are not an obligatory condition for spherulitic growth since decoupling of diffusion with viscosity was not detected for polystyrene spherulites [81, 65]. However, according to the Stokes-Einstein relation, which posits that $D \sim \eta^{-1}$, with D representing the diffusion coefficient and η denoting the solvent viscosity, limited diffusion in fluids is associated with an elevated viscosity. Although this concept specifically applies to fluids, it offers a broader conceptual link between diffusion-limited growth theories that aim to explain the formation of spherulites and the discussion of a required high viscosity.

1.2. Research objectives

Our research sheds light on the ongoing debate on whether spherulitic growth is limited by diffusion or surface integration and the importance of increased viscosity by, for the first time, in-depth experimentally investigating the growth of spherulites. We demonstrate how to induce spherulitic growth of sodium sulfate from evaporative aqueous sulfate salt mixtures. By adding different bivalent ions to a pure sodium sulfate salt solution, we pursue a more general understanding of how to grow spherulites from salt mixtures. Furthermore, we report the critical experimental parameters to control the growth leading to the final spherulitic morphology. The research uncovers insides on the following research questions:

1. How can bivalent ions in sulfate salt mixtures induce spherulitic crystal growth?
2. What growth conditions are required for the growth mechanism that leads to spherulitic growth?
3. By which experimental parameters can we control the growth and morphology of sodium sulfate spherulites from evaporating salt mixtures?
4. Is a critically high viscosity required for spherulitic crystal growth?

1.3. Thesis outline

Before delving into experimental research, a comprehensive literature review is undertaken and consolidated in Chapter 2. This chapter encompasses insights into the morphological variations of crystals, morphological predictions of the equilibrium shape of crystals, the structure and properties of spherulites, fundamental theories of crystallization, and the current state of understanding regarding spherulitic growth. The literature is followed by the method in Chapter 3, which explains in detail the experimental techniques that were used in this research. The experimental results are presented in Chapter 4 and will be discussed in Chapter 5. Finally, conclusions and recommendations are given in Chapter 6. This document ends with the Appendix in Chapter 8 followed by the Bibliography.

2

Theoretical background

2.1. Morphological variations of crystals

For readers new to the field of crystals, this chapter begins with an introduction to lattice symmetry, crystallography, crystal habits, morphological features, and polycrystallinity. By providing this foundational information, we aim to establish a context for understanding the structure and properties of spherulites. The chapter concludes by exploring existing theories on morphological predictions. The final section emphasizes that spherulites cannot be elucidated through equilibrium shape predictions alone. Therefore, the subsequent chapter will delve into the theories of nucleation and growth to understand what thermodynamic and/or kinetic factors are involved in the formation of spherulites.

2.1.1. Lattice symmetry and crystallography

The overall shape of a crystal is strongly influenced by its lattice symmetry. For example, cubic crystals typically exhibit well-defined faces and sharp edges, while hexagonal crystals often form hexagonal prisms or pyramids. The internal structure of a crystal consists of an ordered arrangement of atoms, ions, or molecules. The symmetric nature of crystal systems is characterized by their translational symmetry, where the lattice can be translated by specific vectors while maintaining the same appearance. A single unit known as the unit cell can describe this internal structure. An analogy can be drawn to a mosaic tile, which is the two-dimensional unit cell for a repeating pattern on a mosaic floor. Three-dimensional crystalline structures are described by a set of fourteen distinct lattice types known as Bravais lattices. In Fig. 2.1, are the Bravais lattices grouped into seven crystal systems based on their symmetric features. These lattices form the basis for describing the crystallographic structures of crystals and are fundamental to studying solid-state physics, materials science, and crystallography. Each Bravais lattice is defined by three primitive vectors (a, b, and c) that span the lattice and connect equivalent lattice points. Each lattice point represents an identical atom, molecule, or ion in the crystal structure. The primitive vectors determine the size and shape of the unit cell, which is the basic repeating unit of the crystal lattice. The arrangement of atoms within the unit cell and the crystallographic symmetry together define the crystal structure.

A helpful tool is required to identify prominent crystal faces that may grow at different rates to study crystal growth and symmetry. In crystallography, Miller indices are used to describe the direction of crystal planes. To find the Miller indices of a plane in a crystal lattice, follow these steps: 1) Identify the intercepts of the plane on the crystallographic axes (a, b, c). 2) Take the reciprocals of the intercepts, considering that infinite intercepts are denoted by ”0.” 3) Normalize the indices to obtain the smallest set of whole numbers representing the reciprocal ratios. 4) Enclose the normalized indices in parentheses, using a bar above any negative number. As an illustration, Miller indices are given for three different planes in Fig. 2.2A. In Fig. 2.2B, the Miller indices are identified of the faces of a crystal by imagining its centre at the origin of the coordination system in Fig. 2.2B and performing the steps described above for the planes that the faces are on. Miller indices allow for the description of the internal lattice symmetry and closed-packed planes within the crystal and the external structure (the morphology) of the crystal faces. They are often used in conjunction with a stereographic projection to study the symmetry of the crystal and analyze its crystallographic properties.

Bravais lattice	Parameters	Simple (P)	Volume centered (I)	Base centered (C)	Face centered (F)
Triclinic	$a_1 \neq a_2 \neq a_3$ $\alpha_{12} \neq \alpha_{23} \neq \alpha_{31}$	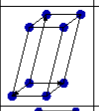			
Monoclinic	$a_1 \neq a_2 \neq a_3$ $\alpha_{23} = \alpha_{31} = 90°$ $\alpha_{12} \neq 90°$	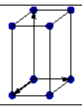	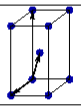		
Orthorhombic	$a_1 \neq a_2 \neq a_3$ $\alpha_{12} = \alpha_{23} = \alpha_{31} = 90°$	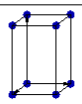	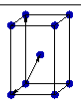	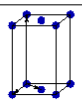	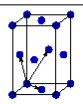
Tetragonal	$a_1 = a_2 \neq a_3$ $\alpha_{12} = \alpha_{23} = \alpha_{31} = 90°$	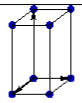	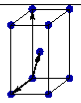		
Trigonal	$a_1 = a_2 = a_3$ $\alpha_{12} = \alpha_{23} = \alpha_{31} < 120°$	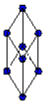			
Cubic	$a_1 = a_2 = a_3$ $\alpha_{12} = \alpha_{23} = \alpha_{31} = 90°$				
Hexagonal	$a_1 = a_2 \neq a_3$ $\alpha_{12} = 120°$ $\alpha_{23} = \alpha_{31} = 90°$	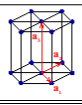			

Figure 2.1: The fourteen Bravais lattices in three dimensions. Source: D.V.Anghel, *Bravais lattice table*, 2003 [57].

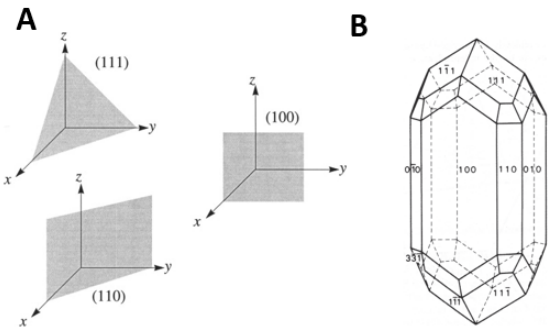

Figure 2.2: A) Three planes are described by their Miller indices. B) Example of a crystal whose faces are identified by Miller planes [40].

2.1.2. Crystal habits

Why do crystals form polyhedral shapes with flat sides, sharp corners, and never spheres? The shape of crystals is characterized by *Steno's law of interfacial angles*, also known as the 'first law of crystallography'. It states that the angles between adjacent crystal faces will always be constant. The sizes of the faces, however, can differ between specimens. Moreover, it might be that a specific face is missing.

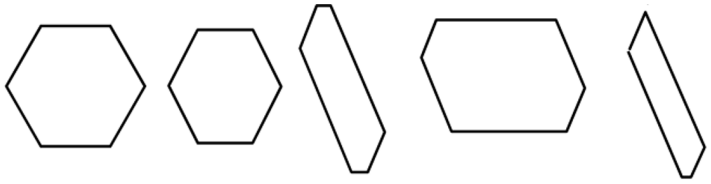

Figure 2.3: Illustration of Steno's law of interfacial angles [63]. All shapes have an angle of 120° between adjacent faces. However, the sizes of the faces can differ. The first four shapes are hexagons. The last shape is a pentagon but can be interpreted as a hexagon with a missing face.

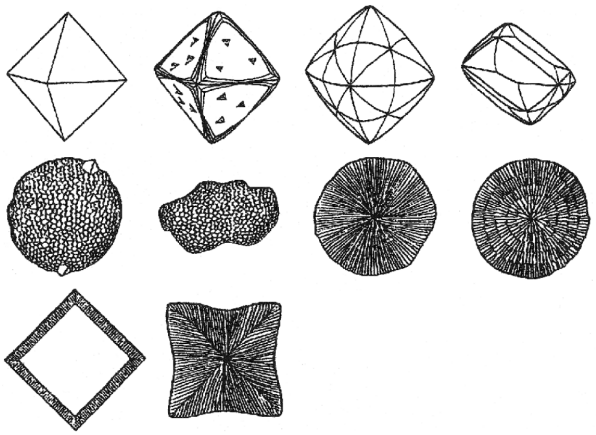

Figure 2.4: Three types of morphologies encountered among natural diamonds [73]

By Steno's law, the angle between the adjacent faces is a characteristic parameter to describe the external structure of a crystal. The characteristic crystal shapes of a crystal or aggregates of crystals that tend to grow repeatedly are referred to as the crystal habit(s), or *habitus*. The crystal habit of diamond for example is an octahedral shape. However, natural diamonds are found in many different morphologies with single crystalline types and polycrystalline types, including spherulites, as shown in Fig. 2.4 [73]. The ability of a material to exist in multiple crystal structures or phases while maintaining the same chemical composition is known as *polymorphism*.

Internal factors such as trapped water molecules within the lattice and external factors such as solvents, supersaturation, temperature and impurities/additives can affect the crystal habits.

2.1.3. The surface-to-volume ratio

Crystals with a high surface area to volume ratio (e.g., very small diameter, very porous, or otherwise not compact) react much faster than monolithic materials because more surface is available.

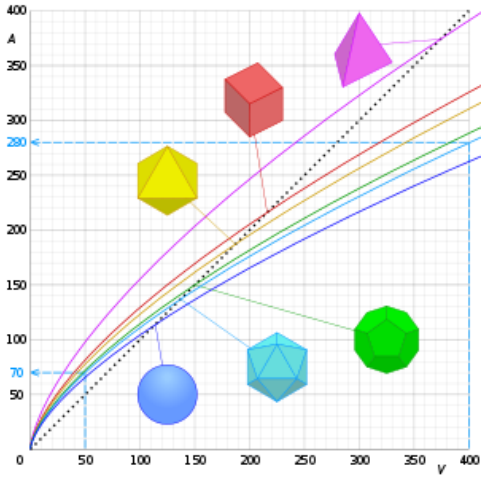

Figure 2.5: Comparison of surface area (A) to volume (V) ratios of different platonic shapes and a sphere [86]. The points where the graphs intersect with the dashed lines indicate that when the volume increases by 8 (2^3), the surface area only increases by 4 (2^2).

In Fig. 2.5, the surface area to volume ratios of different platonic shapes and a sphere are compared [86]. From the graphs, it becomes evident that surface area decreases as the shapes become rounder. Hence, a sphere has the lowest surface area to volume ratio, while needles are at the higher extreme. Additionally, the surface-area-to-volume ratio decreases as the volume increases. The points where the graphs intersect with the dashed lines indicate that when the volume increases by 8 (2^3), the surface area only increases by 4 (2^2). Therefore, surface effects start to play a more dominant role in smaller

scales. For example, nanomaterials are characterized by their typical large surface-to-volume ratio, making their physical and chemical properties significantly different from the bulk [9, 80].
Other common terms that are used to describe crystal morphologies are surface roughness, sphericity and crystal size (or polydispersity). When the surface of a crystal is facetted or rough, the surface-to-volume ratio is relatively larger, and therefore, it will react/dissolve much faster. If a crystal morphology is more spherical, then the surface-to-volume ratio is lower, resulting in a lower reactivity. If there are many small crystals, the reactivity will be higher than if there are fewer but larger crystals. Therefore, the size distribution (polydispersity) is very important for quality requirements.

2.1.4. Polycrystalline aggregates

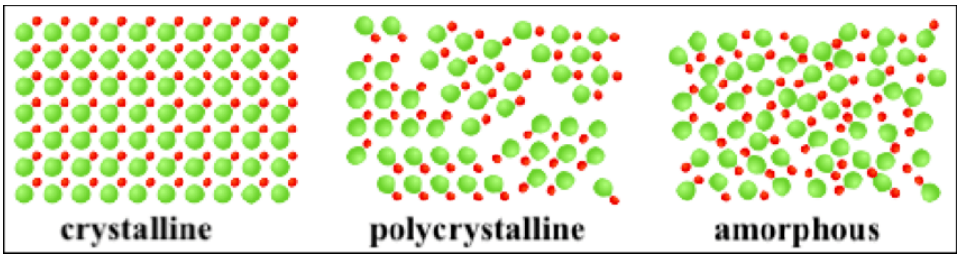

Figure 2.6: Illustration of crystalline, polycrystalline and crystalline structures [14]. From left to right the structure becomes more ordered.

The previous sections have been describing the morphological features of a single crystalline structure so far. However, many crystalline materials, including metals, minerals, snow, and kidney stones, comprise polycrystalline structures. Polycrystalline aggregates are composed of crystal grains with different orientations. Fig. 2.6 illustrates how polycrystalline structures can be placed between the disorder in amorphous structures and the fully ordered crystalline structures. As for single crystals, variations in size, composition, and shape highly influence the properties of polycrystalline materials. Polycrystalline materials often exhibit different morphologies. In Fig. 2.7, the dendrite and varying spherulitic morphologies are listed that are commonly found to be the crystal habits of polycrystalline aggregates [42].

Habit	Schematic
Dendrite	
Spherulite plate	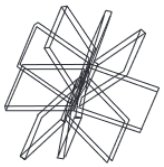
Spherulite blade	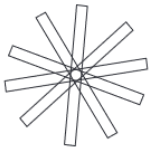
Spherulite needle	

Figure 2.7: Crystal habits of aggregates [42].

2.2. The structure and properties of spherulites

The last section only briefly mentioned that polycrystalline aggregates can exhibit a spherulitic crystal habit. In this section, we delve further into the structure and properties of spherulites and their relevance in various fields.

2.2.1. Spherulitic morphology

Spherulites are not single spherical crystals; they are composed of nanosized polycrystalline aggregates. These highly anisometric crystallites grow from a central parent nucleus and extend radially outward until an outer spherical envelope has developed. The growth pattern of the crystallites resembles rods with dendritic needle-like tips, which split and branch as they progress. The bifurcation angle between a branch and its progenitor is typically between 0°and 15°, and has no relation with the internal crystal structure or symmetry [65]. Besides a needle shape, the branches can take on different morphologies, such as blades (flattened needles) or plates, and may exhibit open or closed structures. Blade spherulites have a flat and elongated morphology with well-defined boundaries (Fig. 2.8a). The radial growth is more prominent in one direction, resulting in a blade-like appearance. Plate spherulites have a more disc-like shape, with the radial growth spreading out in multiple directions, forming plate-like structures (Fig. 2.8b). In this case, they should actually be referred to as cylindrulites. Moreover, spherulites can exhibit a more or less dense morphology called closed or open (or spiky) spherulites [65]. In open spherulites, the branches of the polycrystalline aggregates do not fully connect to each other, leaving spaces or voids between the branches. On the other hand, closed spherulites have a more compact structure with branches that form a continuous network without significant voids (Fig. 2.8c).

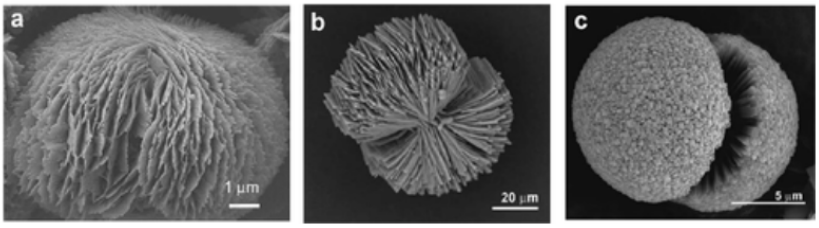

Figure 2.8: Various habits crystallites composing spherulites, illustrated by scanning electron microscope images [65]. a) blade-like, b) plate-like and c) needle-like spherulite.

Spherulites can be classified into two distinct morphological categories based on how they evolve in time [28]. Category I spherulites form by thin needles that grow radially outward from a more or less spherical particle (as shown in Fig. 2.9 on the left). On the other hand, the growth of category II spherulites begins with the formation of a single needle through homogeneous nucleation, which subsequently branches out, resulting in a sheave-like structure (as depicted in Fig. 2.9 on the right). With continued growth, the branching can even cause both ends of the dumbbell-shaped spherulite to meet, forming a spherical shape into a spherical pattern with an uncrystallized region (eye) on each side of the primary nucleation site. Intermediate stages, such as the sheaf-like structures indicated by B,C,D in Fig. 2.9, are often still referred to as spherulites since the same mechanism controls their formation. Besides sheaf-like spherulites, which resemble a bundle of wheat stalks with needle-like branches radiating outward in a more disorganized manner, spherulites often have a dumbbell-shaped intermediate stage.

2.2.2. Crystal optics

Birefringence is an optical property exhibited by certain materials, including crystalline polymers. When light passes through a birefringent material, it splits into two rays with different refractive indices, resulting in double refraction. When these rays pass through a polarizer, like a polarizing filter, the light that vibrates in a specific direction can pass through, while light with other orientations is blocked. When a sample is observed between two crossed polarizers (cross-polarized light microscopy), the birefringent regions in the material become visible as bright and colourful patterns, depending on the crystal orientation and thickness. The colours observed can be correlated with a Michel-Lévy Interference chart, determining birefringence. Birefringence denotes the existence of two distinct refractive indices in the

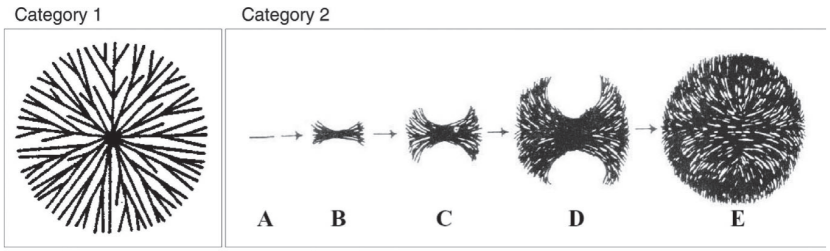

Figure 2.9: Two types of formation of polycrystalline spherulites, by Gránásy et al. [28]. Category 1 spherulites grow radially from the nucleation site and branch intermittently resulting in a space-filling structure. Category 2 spherulites initially grow from thread-like fibres (A, B), to form new branches at the growth front, leading to a sheaf-like structure (C,D) and settling into a spherical pattern with an uncrystallized region (eye) on each side of the primary nucleation site (E).

substance and, while not entirely distinctive, remains a constant parameter that guides in identifying numerous substances.

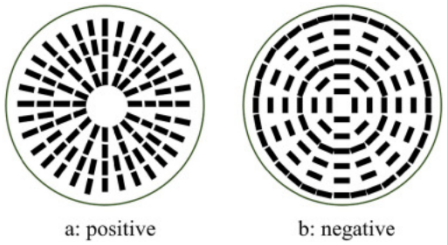

Figure 2.10: Schematic diagram of positive (a) and negative (b) spherulites; the rectangle represents crystalline domain consisting of double helices of starch chains parallel to the long side of the rectangle [64].

Spherulite fibres are recognized by a Maltese extinction cross under cross-polarized microscopic observations, indicating an isotropic orientation of the polycrystalline structure [65]. Furthermore, spherulites are defined optically positive if the orientation and the direction of the largest polarizability are radial (Fig. 2.10a) and optically negative if they are tangential (Fig. 2.10b) [64]. Moreover, many spherulites are characterized by concentric bands. The banded spherulites can be of Type-1 or Type-2 Fig. 2.11. Type-1 spherulites display uniform birefringence colours in adjacent bands, primarily differing shades and optically negative. On the other hand, Type-2 spherulites have noticeably broader bands than Type-1, with two distinct and contrasting birefringence colours (blue and orange) in adjacent bands. Moreover, Type-2 banded spherulites are optically neutral. Interestingly, regardless of temperature variations within the range of 70–85 °C, Type-1 ring-banded spherulites consistently coexist with Type-2 spherulites, and the distinction between Type-1 and Type-2 spherulites remains constant [87].

2.2.3. Reactivity, stability and biocompatibility

Throughout history, spherulites have been reported as undesired anomalies in crystallization processes, mainly in glas and polymer production processes. Spherulites demonstrate a significant surface-to-volume ratio, which can result in various issues, such as instabilities. Nonetheless, these characteristics also render them intriguing for applications that demand high reactivity, solubility, and biocompatibility. For example, spherulites of microbial polyhydroxyalkanoates and high amylose maize starch have been studied for drug release purposes [4, 46]. Moreover, spherulites have been reported to increase the energy conversion energy of photovoltaic cells [45].

2.2.4. Occurrence and observations in various materials

The occurrence of spherulites is a well-established phenomenon in various fields of study. They are commonly found in crystalline materials such as (metal) glasses, polymers and mineral phases [38, 48, 65]. In the comprehensive review of Shtukenberg et al. [65], spherulite-forming substances are listed that are grown from the melt, from solids, solutions and gels. Various materials are described to exhibit spherulitic growth under the right conditions, including small molecule organic crystals, high-polymers,

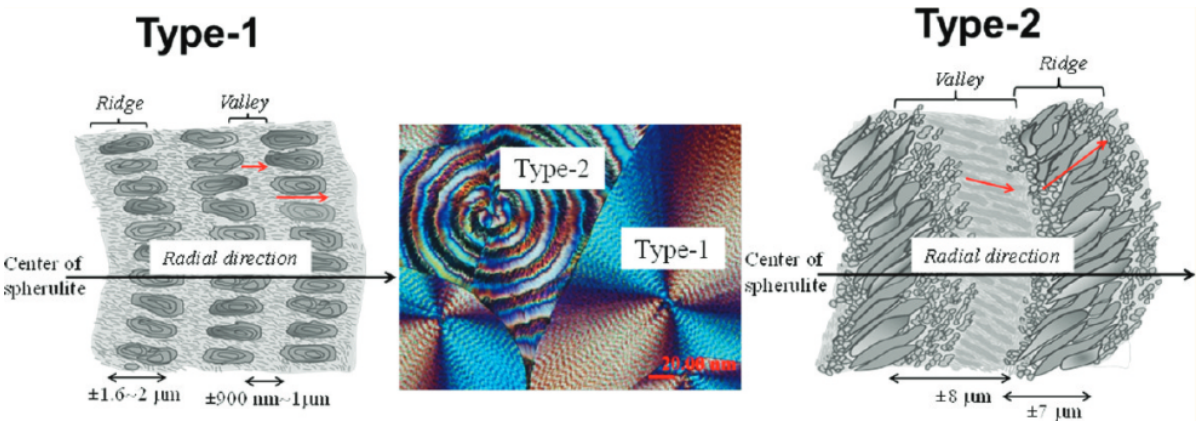

Figure 2.11: (a) POM graphs of Type-1 and Type-2 spherulites in PNT films melt-crystallized at 85 °C (middle); and schemes for AFM-analyzed morphology details in (left) Type-1 (Tc = 70−85 °C) and (right) Type-2 (Tc = 80−85 °C) ring- banded spherulites of polynonamethylene terephthalate (PNT) [87].

minerals, elements, inorganic (salt) crystals, metals, and reheated glasses. The extensiveness in which spherulites are observed lends strong support to the argument that any crystalline material has the potential to form a spherulitic morphology. Further details and references to the literature for specific compounds are readily found in the mentioned review on spherulites [65].

2.2.5. Relevance in diverse fields

As previously mentioned, spherulites are found in various types of materials. A fundamental understanding of the growth mechanism of spherulites will, therefore, contribute to crystallization processes in polymers and glasses and may also lead to pharmaceutical and photovoltaic innovations. However, the growth mechanism of spherulites is of particular interest in the medical field. For example, studies on kidney stones have found that they exhibit a spherulitic texture [67, 5]. Understanding the growth mechanism of spherulitic crystallization could lead to developing new strategies for preventing kidney stone formation. Furthermore, the formation of spherulites is also of particular interest for amyloid disorders, such as Alzheimer's disease [39]. Spherulite amyloid structures are even recognized by their typical "Maltese-cross" extinction pattern (see section 2.2.2) for pathological diagnosis [32]. Moreover, spherulites are also found in mineralization between collagen fibres in bones [47]. However, the study of spherulites is not limited to the smaller scales. Meters-wide megaspherulites that are formed in rhyolitic lava have been of interest to mineralogical and geochemical investigations [11]. For this application, the spherulitic formation can be used to indicate the geothermal history of effusive rocks [22].

2.3. Morphological predictions of the equilibrium shape of crystals

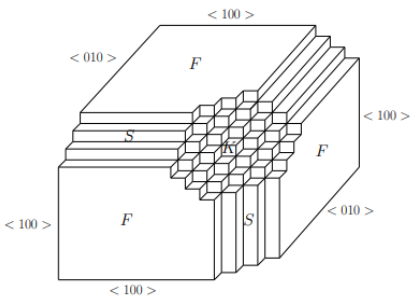

Figure 2.12: Illustration of F (flat) faces, S (stepped) faces, and K (kinked) faces [54]

This section serves as an introduction to the most well-known theories relevant to morphological

predictions. We explain how crystal faces have different surface energies and how surface free energy energy is used to construct a Wulff-plot. However, it is essential to note that the equilibrium shape predictions discussed herein often fall short in explaining complex structures.

2.3.1. Classification of crystal faces

Crystal faces are important for morphological predictions since the equilibrium shape of a crystal will be governed by the crystal faces with the lowest specific surface energies. There are three types of faces:

- F (flat) faces: These are parallel to at least two dense atomic rows
- S (stepped) faces: These are parallel to at least one dense atomic row
- K (kinked) faces: These are not parallel to any dense atomic rows

The three types of faces are illustrated in Fig. 2.12.

The F, S, and K faces will atomically grow by different mechanisms. This can be understood from the sites of crystal surfaces that are classified by the terrace-ledge-kink model (also known as the Kossel and Stranski model) based on the number of saturated bonds:

Position of atom	# of saturated bonds
Within face (surface/terrace atom)	5
Within step (ledge atom)	4
Within kink (kink atom)	3
Weon step (ledge adatom)	2
Upon face (Adatom)	1

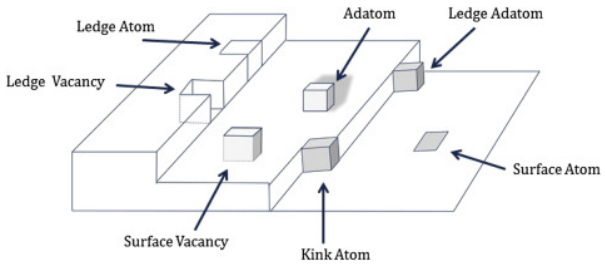

Figure 2.13: TLK model : classification of surface sites [89]

The more saturated bonds the surface site has, the lower its surface energy is.

2.3.2. Surface free energy and interfacial surface tension

Droplets of a phase surrounded by another phase can exist if the internal pressure acting on the cross-sectional area (p [N $m^{-}2$]) is not exceeded by the surface tension γ with the surrounding phase. In a sphere, the cross-sectional area is πr^2. Balancing forces gives

$$\pi r^2 p = 2\pi r\gamma, \tag{2.1}$$

And therefore

$$p = \frac{2\gamma}{r} \tag{2.2}$$

The surface tension along the perimeter of the droplet $2\pi r$ [$Nm^{-}1$] is the surface energy per unit area [$Jm^{-}2$] or the work required to create a unit of interface for solid/vapour and liquid/vapour interfaces. However, for liquid/liquid, solid/solid and liquid/solid interfaces, the work required to create a unit of interface is described by the interfacial tension σ [$Nm^{-}1$] that is given by Young's equation:

$$\sigma = \gamma_{LV}\cos\theta = \gamma_{SV} - \gamma_{SL}, \tag{2.3}$$

where γ_{SV} is the solid surface free energy, γ_{LV} is the liquid surface free energy, γ_{SL} is the solid-liquid interfacial free energy and θ is the contact angle (Fig. 2.14A).

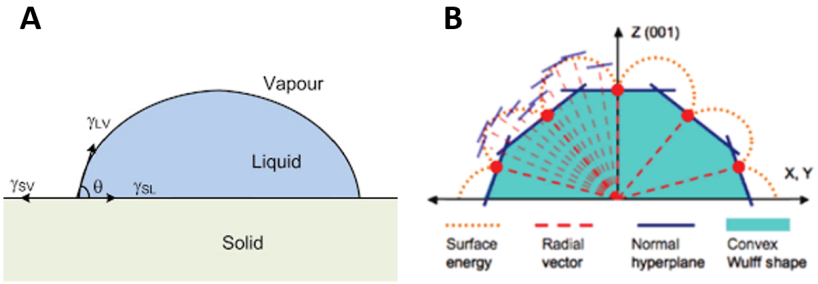

Figure 2.14: A. Schematic representation of Young's equation B. Wulff-plot [49]

In liquids and gasses, the interfacial tension is isotropic. The lowest energy form will be the one minimizing the surface area. Hence, liquid droplets and gas bubbles have a spherical form. However, in crystals, the interfacial tension is anisotropic. The surface energy at angle $\theta, \gamma(\theta)$, is related to the expected crystal shape by the Gibbs-Wulff theorem:

$$\Delta\left(\sum_i \gamma_i A_i\right) = \sum_i \gamma_i \Delta A_i = 0 \tag{2.4}$$

2.3.3. Wulff-plot

There are two approaches to predicting the shape of a crystal [84, 17]. From a thermodynamic approach, the Wulff-Construction predicts an "equilibrium" crystal habit, while the Frank-Chernov construction considers kinetic factors of individual faces to predict the steady-state "Growth" habit.

A crystal has different facets that can have varying surface energies. The higher the surface energy of a facet, the faster it grows. The facets that grow fast will be eliminated while the more slowly growing facets will dominate at the end of the growth period in the morphology. Therefore, it is possible to predict the equilibrium shape of the crystal based on the Gibbs-Wulff theorem given in equation 2.4.

$$\frac{\gamma_1}{H_1} = \frac{G_2}{H_2} \cdots = \frac{\gamma_i}{H_i} = \cdots \frac{\gamma_N}{H_N} \tag{2.5}$$

The equilibrium shape can be constructed by what is called a Wulff-plot (Fig. 2.14B). The orange line in Fig. 2.14B is the surface energy plotted over different directions. To find the equilibrium shape, one must draw the normal of the radial vector (r) at each point on the surface energy plot (blue lines). The resulting inner volume then gives the equilibrium shape.

Due mainly to Frank and Chernov, the classical kinematic theory of crystal growth provides a mathematically equivalent prescription for the steady state growth shape. This criterion, known as the Frank-Chernov condition, applies to faceted crystals with N faces on their surface. While the Wulff construction is used to determine equilibrium shapes, the Frank-Chernov condition replaces the specific surface energy of a face with its respective normal growth rate. The condition is therefore expressed as a constant ratio between the growth rates (Gi) to the perpendicular distances (Hi) of each crystal face from an internal reference point within the crystal:

$$\frac{G_1}{H_1} = \frac{G_2}{H_2} \cdots = \frac{G_i}{H_i} = \cdots \frac{G_N}{H_N} \tag{2.6}$$

The condition also applies to the dissolution process, wherein dissolution rates replace the growth rates.

.

2.4. Crystallization fundamentals

Crystals can be formed by two types of phase transitions, from liquid to solid or from vapor to solid. The pathway (in terms of changing environmental conditions) during the phase transition plays an important role in the morphological development of the crystal. Phase diagrams provide the foundation

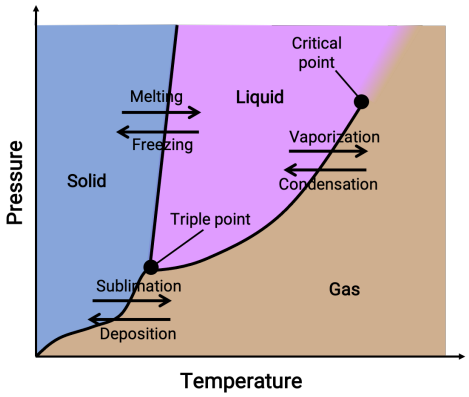

Figure 2.15: A simplified P-T phase diagram [21]

for understanding the behavior of materials during solidification. In Fig. 2.15, a simplistic version of a pressure-temperature (P-T) phase diagram is presented, which is similar to the phase diagram of water in which the solid would be ice. Cooling water until the line between the liquid and solid phase is crossed will initiate the formation of ice crystals. Besides pressure and temperature, there can be other variables presented on the axis of a phase diagram, such as composition or relative humidity. Moreover, phase diagrams usually get much more complex, for example, for binary systems and materials that are known to have multiple solid phases, such as salt hydrates. To understand by which mechanism a liquid-solid or vapour-solid phase transformation occurs and what factors can influence crystal formation, we must delve into crystal growth theories.

The classical nucleation growth model, as illustrated in Fig. 2.16, delineates the formation of crystals upon a dynamic process such as solvent evaporation, into three distinct stages: (I) solute accumulation, (II) nucleation, and (III) growth. However, it is essential to recognize a fourth stage which is often overlooked, which entails the agglomeration of growing crystals, known as Ostwald Ripening. The significance of this stage varies depending on the specific system under consideration. The initial stage, nucleation, serves as the cornerstone of crystal growth. This stage represents a stochastic process, where atoms, molecules, or ions, driven by random motion, coalesce to form clusters. These clusters then aggregate or evolve into embryo-like structures. These embryos ultimately combine to create well-organized nuclei, commonly referred to as seed crystals, from which the subsequent crystal growth can continue.

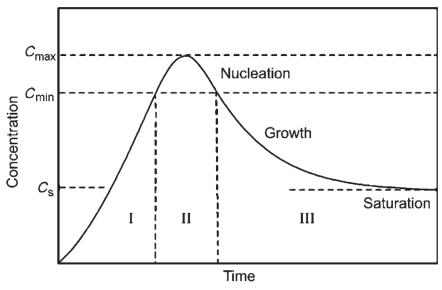

Figure 2.16: LaMer and Dinegar's model that describes three stages of nucleation an nucleus growth [24]: I Solute built up, II nucleation, III growth. Ones the concentration is stabilized again at the solubility concentration (Cs) Ostwald ripening can occur.

This chapter will explain the relevant classical and nonclassical concepts that form the foundation of nucleation and growth. At first, we delve into the fundamental thermodynamic principles of which the most established nucleation theories are derived. Subsequently, the diverse growth mechanisms that are limited by the surface integration or diffusion of atoms are outlined. Finally we discuss the relation between the different types of growth mechanisms and crystal morphologies.

2.4.1. The chemical potential difference as driving force

As mentioned before, the creation of new surfaces and interfaces requires work. In crystallization processes, the barrier for a phase transformation can be overstepped by inducing a driving force that drives the transport of solute from the bulk to the crystal surface. At the surface, the solute gets oriented and integrated into the crystal lattice. When a liquid phase crystallizes into a solid phase, the thermodynamic driving force for the phase transition is represented by the difference between the chemical potentials of the phases.

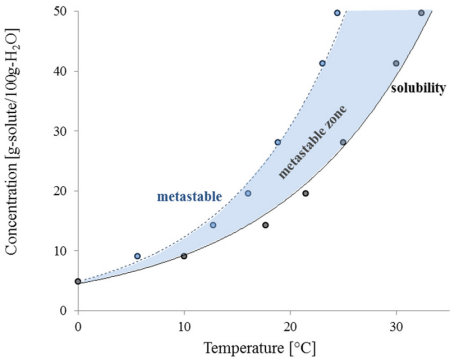

Figure 2.17: Solubility line and metastable zone for sodium sulfate decahydrate (mirabilite) in water [30].

In Fig. 2.17, the solubility phase diagram of mirabilite (the hydrated phase of sodium sulfate) is presented. At the equilibrium lines in a phase diagram, the chemical potentials of the phases are equal. Above the solubility line, the solution is oversaturated and the salt will start to precipitate (solidification). The driving force of the concentration is $\Delta c = c - c^*$, expressed as the difference between the concentration of the solution (c) and the concentration of the saturated solution (solubility) at a given temperature (c*). The barrier for a phase transformation to occur is, in reality, not really a thin line as presented in the phase diagrams but a nucleation zone. This is referred to as the metastable zone, which is also illustrated in Fig. 2.17. Impurities or seed crystals can reduce the width of the metastable zone, resulting in a more controlled nucleation. However, the concentration can reach far above the solubility under certain conditions, meaning that the solution is supersaturated. Crystallization at high supersaturation typically leads to the formation of small crystallites, droplets, or bubbles and clusters with a large surface area to volume ratio. The supersaturation is given by the ratio $\mathrm{S} = \frac{c}{c^*}$, and the relative supersaturation is $\sigma = \frac{\Delta c}{c^*} = S - 1$. The chemical potential difference $\Delta\mu$ can then be expressed as a function of the supersaturation:

$$\Delta\mu = RT * ln(S) \tag{2.7}$$

For ionic species (ions in a solution) the expression becomes:

$$\frac{\Delta\mu}{RT} = \nu \ln \frac{a_{\pm}}{a_{\pm,\mathrm{eq}}}, \tag{2.8}$$

ν ions, being the sum of ν_+cations and ν_-anions and $a_{\pm}$is the mean activity of the ionic species, resulting from the correction of the free concentration of ions, c, by the mean activity coefficient, $\gamma_{\pm}$. The activity coefficient can be estimated by different models, depending on which is appropriate for the specific solution. Often the concentration is replaced by a dimensionless number called the activity. The activity is the effective concentration that is given by $a_{solute} = \frac{C}{C^\circ}$, where C° is the standard state for solute concentration and usually 1 molal (moles solute/kg solvent).

As mentioned before, nucleation is a stochastic process and therefore it is more likely for phase transformation to occur when the driving force is higher. In terms of supersaturation, this means increasing the concentration with respect to the solubility, $\Delta c = c - c^*$. Another way to increase the driving force is to decrease the temperature of the solution until a point where the solution becomes supercooled. The degree of supercooling (also referred to as undercooling) is then defined by the difference between the temperature and the melting temperature, $\Delta T = T - T_m$. In Fig. 2.18 this is illustrated for sodium sulfate decahydrate, with a graph of the critical radius of sodium sulfate decahydrate as a

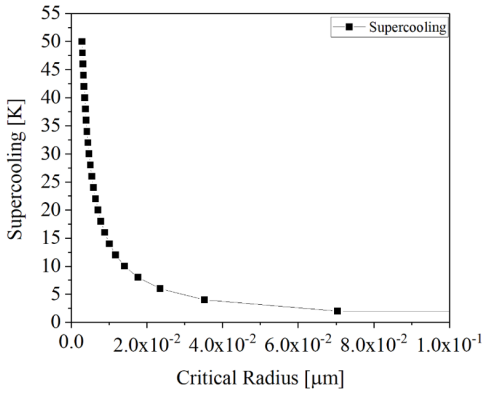

Figure 2.18: Critical radius as a function of the supercooling of sodium sulfate decahydrate (mirabilite). The surface tension γSL: 74 erg/cm, Latent heat: 240 J/g, Tm: 32.4 °C [26].

function of the supercooling. The higher the degree of supercooling, the smaller the critical radius for nucleation will be.

2.4.2. Nucleation theories

In the preceding section, we discussed the driving force behind nucleation. The thermodynamic fundamentals behind nucleation and growth theories rely on the principle of energy minimization, which is evaluated by the change between Gibbs free energy (ΔG) between two phases. The change in Gibbs Free energy during the nucleation process is the sum of free energy due to the formation of new volume (ΔG_{V}) and the energy barrier to create new surface (ΔG_{S}) :

$$\Delta G = \Delta G_{\mathrm{V}} + \Delta G_{\mathrm{S}} = -\frac{4}{3}\pi r^3 \rho_{\mathrm{s}} T \Delta\mu + 4\pi r^2 \sigma$$

where $\Delta\mu$ is the chemical potential difference, σ is the specific free interface, r the radius of the growing nucleus and ρ_{s} the density of the precipitating compound. Fig. 2.19 gives the free energy profiles in relation to the radius of the nucleus. While the volume energy minimizes the change in Gibbs free energy, the surface energy is repressing the formation of a stable nuclei. However, the volume energy depends on the radius with the power of 3 while the surface energy only grows with a power of 2. The overall free energy during nucleation (green line) will be at a maximum, at a certain critical radius r^*. The critical radius relates to the specific free interface and chemical potential difference by:

$$r^* = \frac{2\sigma}{p_{\mathrm{s}}|\Delta\mu|}$$

Nuclei sizes with $r > r^*$ will further grow and form stable entities as they can overcome the activation energy barrier which is equal to the critical change in Gibbs free energy (G^*), at the critical radius. One can see directly from the formula's that the larger the chemical potential difference is, the *more likely* it is that the critical radius will be reached. Therefore, the chemical potential difference is also referred to as the driving force for nucleation.

Classical nucleation theory (CNT) describes two types of nucleation, homogeneous and heterogeneous nucleation. Homogeneous nucleation is the ideal case in a pure environment without any foreign particles or precipitates where only spontaneous nucleation can happen. The rate of homogeneous nucleation, J_{hom}, is given by the following Arrhenius-type equation [76]:

$$J_{\mathrm{hom}} = A_{\mathrm{hom}} \exp\left(\frac{-\Delta G_{hom}}{k_B T}\right) = A_{\mathrm{hom}} \exp\left(\frac{-16\pi\gamma^3 v_c^2}{3k_B^3 T^3 (\ln S)^2}\right) \tag{2.9}$$

where A_{hom} is a pre-exponential factor that depends on the attachement kinetics, γ is the surface energy, v_c is the crystal atomic volume, S is the degree of supersaturation, T is the temperature, k_B and is the Boltzmann's constant.

However, homogeneous nucleation is rare and happens only at extreme high supersaturations. In most scenarios, primary nucleation is of the heterogeneous type, meaning that it involves the aggregation of particles with the aid of foreign objects (such as dust or interfaces). Due to the already existing surface of the foreign object, the Gibbs free energy (ΔG*) is lower compared to homogeneous nucleation. To account for this, heterogeneous nucleation considers an extra surface tension term for the presence of foreign particles, which is usually expressed with activity factor which can vary between 0 and 1 ($\zeta (0 < \zeta < 1)$):

$$J_{\text{het}} = A_{\text{het}} \exp\left(\frac{-\Delta G_{\text{het}}}{k_B T}\right) = A_{\text{het}} \exp\left(\frac{-16\pi\gamma^3\zeta^3 v_c^2}{3k_B^3 T^3 (\ln S)^2}\right) \tag{2.10}$$

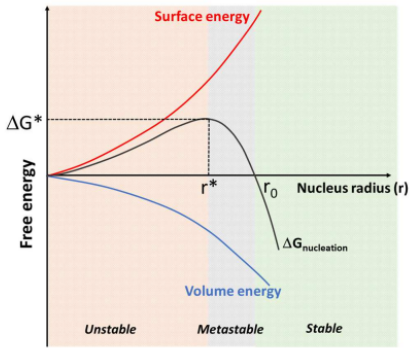

Figure 2.19: Schematic of the critical radius as a function of the Gibbs energy barrier for nucleation ΔG* (black line) [60]. The Gibbs free energy is dissected in the surface energy (red line) and volume energy (blue line). Unstable, metastable and stable domains are colored in orange, grey and green respectively.

The classical nucleation theories explained above are concerned with primary nucleation, were crystals are formed from a clear solution. Conversely, in the case of secondary nucleation the nuclei are formed at the growth front of an already stable crystal, such as seed crystals. Therefore, secondary nucleation is also sometimes referred to as growth front nucleation (GFN) [29]. Secondary nucleation is often preferred in industrial processes since it is a more predictable form of nucleation.

The rate of secondary nucleation is given by:

$$J_{\text{sec}} = A_{\text{sec}} C_s^a (S-1)^b \tag{2.11}$$

where A_{sec} is the rate constant of secondary nucleation and C_s is the concentration in the solution [76].

While the conventional crystallization model depicts a direct and swift transition from an amorphous or liquid state to a crystalline state, recent findings of intermediate metastable states emerging before reaching a stable state challenge this perspective. Particularly in the context of nanocrystal synthesis, classical frameworks prove insufficient in describing the intricacies of nucleation processes. Consequently, alternative nucleation pathways are proposed, with two prominent alternatives being stepwise nucleation and nucleus aggregation [53]. In Fig. 2.20, stepwise nucleation, aggregation of nuclei and a mix of these two nucleation pathways are compared to the classical nucleation model.

In the case of classical nucleation through atom-by-atom addition, a nucleus has to overcome the energy barrier ΔG. In Fig. 2.20, the pathway that is predicted by the CNT is indicated with red dotted curves. The schematic in Fig. 2.20 illustrate other non-classical nucleation pathways, namely:

- *Nucleation by aggregation of subcritical clusters*, which considers that when two or more subcritical clusters merge, they will form a nucleus beyond the critical size, circumventing the high-energy barrier (blue arrow). The surface energy is lowered by the aggregation, and therefore, the system's free energy decreases (Fig. 2.20b).

- *Stepwise nucleation* that passes through one or several metastable or partially ordered states before reaching the final stable crystalline phase. These intermediate states are often referred to as ”precursor phases” or ”clusters” and are typically characterized by a lower degree of order or crystallinity than the final crystal. The intermediate state reduces the interfacial energy, thereby substituting the high-energy nucleation barrier as predicted by classical nucleation theory (CNT) with lower energy barriers, as indicated by the black curves in Fig. 2.20c.

Fig. 2.20d represents a combination of coalescence of subcritical clusters and stepwise nucleation that lower the free energy in a complementary way.

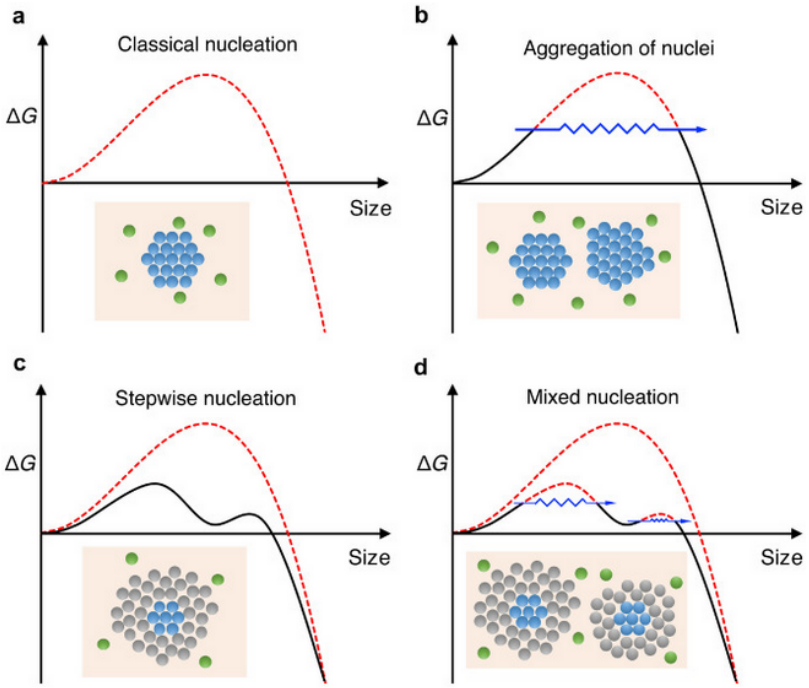

Figure 2.20: Schematic of the free-energy change due to nucleation ΔG with the evolution of the nucleus by different pathways [53]. The dashed red curves predicted by the CNT are avoided by nonclassical nucleation pathways. (a) Classical nucleation through atom-by-atom addition, (b) Nucleation by aggregation of subcritical clusters, c) Stepwise nucleation involving an intermediate state between the parent and product phases, (d) Nucleation combining coalescence of subcritical clusters and stepwise nucleation. Colours of atoms represent phase structures: green-parent phase; grey-intermediate state; blue-product phase.

2.4.3. Growth mechanisms

Crystal growth theories are concerned with the growth of crystal nuclei to macroscopic dimensions. This section will discuss the two classical crystal growth theories, diffusion-controlled and intergration-controlled growth. Diffusion-controlled growth is when the growth of the solid phase is limited by the diffusion of latent heat away from the solidification front or the diffusion of atoms/molecules towards the solidification front. Integration-controlled growth is limited by the rate at which particles/atoms can align themselves to be incorporated in the crystal lattice at the surface. As will be elaborated on in this section, it depends highly on the supersaturation which of the two will be the limited factor for growth and therefore the governing growth mechanism.

If the supersaturation is too low for diffusion-controlled growth, then growth can still take place integration-controlled growth mechanisms. Integration-controlled growth is homoepitaxial when the crystal grows on a substrate or surface of the same material. Homoepitaxial growth knows a roughnening transition from lower driving force resulting atomically smooth interface (spiral and two-dimensional growth) to higher driving forces, resulting in an atomically rough interface (adhesive growth). The growth rate of intergration controlled growth is constant with the radius (r) and time (t) [65]. Meaning

that the size of a crystal growing by integration-controlled growth is linear in time:

$$r \propto t$$

The growth rate of the three homoepitaxial integration-controlled mechanisms are all derived from the power law relationship that is commonly used to describe the overall growth rate,

$$G = k_{\mathrm{g}} \left(S_{\mathrm{a}} - 1\right)^{g}$$

where S_{a} is the activity-based supersaturation ratio, and k_{g} is the temperature-dependent growth rate constant. The value of g has a typical value for each of the different growth mechanisms [3].

At supersaturations lower than the critical value for surface nucleation, growth can still take place due to stacking faults in the crystal lattice that lead to skrew dislocations. A skrew dislocation provides a step (or edge) that can act as a site for furhter growth. Spiral growth is then initiated by the attachement along the inherent skrew dislocations, by which the face eventually propagates outwards by a spiral mechanisms [3]. The value of g=2, resulting a parabolic law for the growth rate, R:

$$R = A(\Delta\mu/kT)^2 \tag{2.12}$$

where A is a constant and $\Delta\mu/kT$ is the driving force.

When the supersaturation is increased to a point where it overcomes the energy barrier, steps will nucleate around a two-dimensional island by attachment to the edge (Fig. 2.21). By the increase of the nucleation rate, the surface will become rougher, allowing for units to be intergrated anywhere. The growth rate, R, is governed by the exponential increase of the nucleation rate and therefore described by:

$$R = A\exp(-B(\Delta\mu/kT)) \tag{2.13}$$

where B is another constant.

The two mechanisms for integration-controlled growth mentioned above, spiral-defect and two-dimensional growth, involve the addition of new material mainly at steps and kinks on the crystal surface, resulting in large flat regions. However, if the supersaturation level is even higher and the driving force is reaching another critical point, deposition of material becomes favorable even on flat surfaces without the need for edges or kinks. Which is known as adhesive or rough growth. The growth rate of rough growth follows:

$$R = A(\Delta\mu/kT) \tag{2.14}$$

Integration-controlled growth can also be governed by a foreign substrate on which a new layer of crystal is forming, which is called heteroepitaxial growth. Three modes of heteroepitaxial growth are distinguished: Layer-to-Layer (FM), Island growth (VW) and layer-plus-island (SK) [75]. The growth rate of heteroepitaxial growth depends on multiple factors such as the Deposition Incoming Flux F, Adatom Incorporation Rate T, Surface Diffusion Current Density $\vec{J}$, Thermodynamics Chemical Potential μ and Film Strain ε. Therefore it is only possible with continuous modeling to predict the growth rate [79].

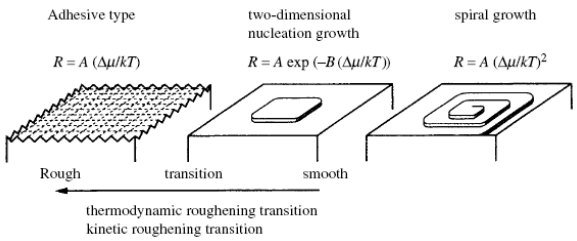

Figure 2.21: The roughening transition from crystal growth. From lower driving force resulting atomically smooth interface (spiral and two-dimensional growth) to higher driving forces, resulting in an atomically rough interface[73].

Instead of integration-controlled growth the growth becomes mass-transfer controlled by diffusion from the bulk liquid, at even higher supersaturations. Mass-transfer a diffusive-limited growth problem, diffusive growth has a parabolic time dependence [65]:

$$r \propto t^{1/2}$$

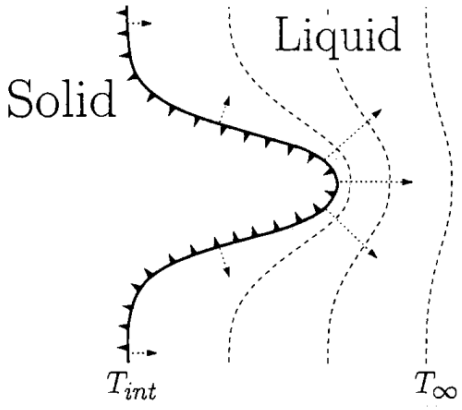

Figure 2.22: The Mullins-Sekerka instability [59] At the top and the bottom the interface is stable while in the middle the diffusion field moves in perpendicar direction ahead, increasing the surface and therefore the entering flux of particles. This will lead to a faster growth at the perturbed region of the interface.

The rate of mass deposition, R during crystal growth is:

$$R = \frac{1}{A}\frac{dW}{dt} = k_G\,(c - c^*)^g\,, \tag{2.15}$$

where W = mass of crystals per volume of solvent A = surface area of crystals per volume of solvent kG = overall mass transfer coefficient (depend on T, crystal size, hydrodynamic conditions, and presence of impurities.) g = the order usually between $0 - 2.5$ (near unity is most common).

Another form of diffusion-controlled growth is when the growth is limited by heat transfer. However, in general $D_{\text{heat}} \gg D_{\text{solute}}$, and therefore heat transfer is rarely a limiting factor for the growing front [59]. However, both types of diffusion can have a destabilizing effect of the growth front. The destabilizing effect will be competing with the stabilizing effect of the surface tension, leading to protrusions in at the growth front. This phenomena is referred to as the Mullins-Sekerka instability [51]. This model proposes a characteristic wavelength between the perturbations by the following formula:

$$\lambda \sim 2\pi\sqrt{d_0 l_D}$$

where d_0 is the capillary length and $l_D \equiv 2D/v$ is the diffusion length. By this model several interface phenomena are explained such interface instabilities caused by constitutional supercooling, dendritic growth and sidebranching.

We described above that crystal growth can be limited by diffusion or by integration kinetics, with the typical scenario falling somewhere in between. But how does the growth affect the crystals' morphologies? In 1990, Sunagawa presented a schematic diagram in his report on the morphological characteristics of diamond crystals under stable and metastable conditions that explain how the different morphologies of a crystal are related to the growth rate and driving force [72]. Herein, different crystal forms (such as polyhedral, hopper, and dendritic) are related to their growth mechanisms (Fig. 2.23). The growth mechanisms are represented by three curves: curve A signifies spiral growth, curve B indicates two-dimensional nucleation growth, and curve C represents the adhesive-type growth mechanism. With stars, the critical transition points from smooth to rough growth are indicated. While smooth growth such as spiral or two-dimensional growth leads to polyhedral and hopper shapes, rough growth is associated with dendritic, fractal, and spherulitic morphologies. According to this schematic, spherulitic radiating aggregation is expected at large driving force (supercooling or supersaturation). While it is widely accepted that spherulites grow under high driving forces without contradiction, the specific conditions and mechanism governing the growth rate remain under discussion.

Let's conclude this chapter with the note that although the growth can be dominated by one or the other mechanism that is described above, they will always coexist. In the upcoming chapter, we will delve into the current understanding of spherulitic growth, revealing that the distillation of the mechanism for spherulitic growth is a more complex task than initially anticipated.

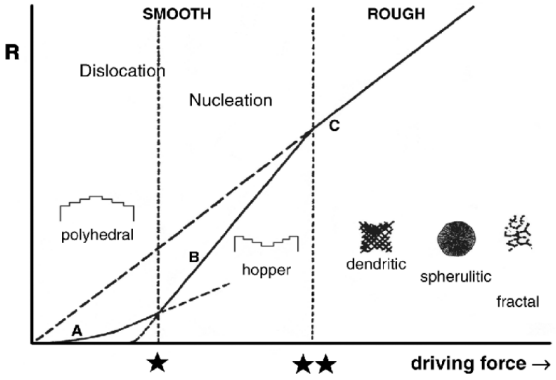

Figure 2.23: Different crystal shapes, both in single crystals (polyhedral, hopper, dendritic) and polycrystalline aggregates (spherulitic and fractal), are influenced by various factors such as growth rate (R), driving force, interface roughness (smooth and rough), and growth mechanisms. The growth mechanisms are represented by three curves: curve A signifies spiral growth, curve B indicates two-dimensional nucleation growth, and curve C represents adhesive-type growth mechanisms. The critical points marked as * and ** are where the predominant growth mechanism undergoes a change [73].

2.5. Current understanding of spherulitic growth

Although there isn't a universally agreed-upon theory for spherulite crystallization, several phenomenological models and essential physical conditions for this phenomenon have been proposed. This chapter will provide an outline of the growth conditions and mechanism of spherulites that were proposed throughout the last century. These theories originate often from the field of viscous fluids and polymers where spherulites have emerged as a focal point of considerable interest and research. However, the question remains whether they describe a general theory for spherulitic growth.

2.5.1. Growth mechanism of spherulites

In the first section spherulites were distinguished in two categories: category 1 spherulites that grow from a nucleation point radially outwards while occuring branches fill up the intermediate space, and category 2 spherulites that initially grow as fibers (needles) that will branch out at the tips forming sheaf-like structures [28]. However, category 1 spherulites are probable manifestations of category 2 spherulites but with nuclei that are too small to be seen with the current microscopic observation methods [65]. The following two phenomena are characteristic for spherulitic growth:

- Thin needle-like crystals growing radially outwards (referred to as splay)
- Non-crystallographic branching at the growth front

Non-crystallographic branching means that the branches have different orientations compared to each other. This phenomenon distinguishes spherulites from dendrite formation and twinning in which there is a relation between the grain orientations. This section will elaborate on the mechanisms and theories that were believed to explain these two phenomena.

Consititutional supercooling and Mullins-Serkerka instability

In 1963, Keith and Padden suggested that the presence of static heterogeneities (including impurities, molecular defects, and mass polydispersity in polymeric materials) can lead to the exclusion of these components from the growing front, forming channels similar to those seen in eutectic structures [34]. Therefore, constitutional supercooling, which reduces local melting points by impurities leading to protrusions in the growth front, was designated by them as the appropriate mechanism for the branching of spherulites. These protrusions are approximately at the scale of the diffusion length θ. Fibers are formed by this phenomena from the protuberances through the throughs between the outgrowths of which the diameters δ can be estimated by the ratio between the coefficient of self-diffusion and the growth rate, δ = D/G.

Additionally, Keith and Padden proposed that fibril formation through interface instability serves as a mechanism for non-crystallographic branching. This theory lasted for many years mainly because of

the applicability of heterogeneous nucleation processes. However, the theory was rejected after quantitative microscopy of individual lamellae or lamellar stacks in polyethylene (PE) spherulites revealed that the observed feature size was not directly proportional to the diffusion length but significantly smaller. The theory gained attention again when Goldenfeld generalized the constitutional supercooling model in terms of the Mullins-Sekerka instability in 1987. The Mullins-Sekerka instability considers perturbations at the growth front whose advancement depend on heat transfer or diffusion (see section 2.4.3). He concluded that the size of fibrils has to be proportional to $\delta \propto (D/G)^{\frac{1}{2}}$ not D/G. It was then believed that diffusion-controlled growth can account for the occurrence of spherulites, their small-angle non-crystallographic branching, and the linear form of their radial growth rate.

Non-crystallographic branching
Ryschenkow & Gaivre discussed in 1988 what the underlying factors are of the non-crystallographic branching of spherulites [58]. First of all, several spherulitic modes of crystallization have been observed to coexist at a similar undercooling of the liquid. The presence of the multiple spherulitic modes indicates the presence of several stable conditional states for the small-angle branching phenomenon. Bisault, Ryschenkow & Gaivre explained this by a mechanism that promotes polygonization of crystal during growth (small-angle branching) [8]. During moderate undercooling of the liquid, the small-angle branching intermittently initiates a homoepitaxial large-angle branching. Furthermore, from observations of spherulites crystalling from amorphous films, it became clear that dislocations should play a significant role. In fact, they conclude that crystal inhomogeneity, dislocations, and stress are the underlying factors of non-crystallographic branching. This correlation has been experimentally confirmed for a variety of crystals that are listed in the review of Shtukenberg et al. [65]. With phase field modelling Gránásy et al. [27] explain how introducing static heterogeneities (foreign particles, dirt) perturbs the formation of monocrystals by deflecting the growing tips.

Parralel to this, two competing theories were being devised both aimed to explain the divergence (or splay) of spherulite fibrils as they extend radially outward. First, Tiller [77] extended the Mullins-Serkerka instability model to account for density differences between the growing crystal and surrounding liquid. Tiller's idea is that when a solid and a liquid with distinct densities come into contact and freeze, they induce liquid movements; if the solid is denser than the liquid, a flow will move towards the front of the freezing interface. This hydrodynamic model can be applied to all materials and explains the radial splay by a hydrodynamic scaling factor. However, from the field of polymer science another mechanism is then believed to cause the splay, that relates to imperfections in the polymeric folding process [55, 35]. According to Basset et al.[6] the entropic pressure of dangling ends caused by imperfect folding promote lamellae to bend in radial directions [20, 1]. However, this theory only applies to spherulites grown from a polymeric melt and does not explain the occurance of spherulites observed without the presence of polymers. Later, Basset et al. [6] identified also another mechanism and conclude that the divergence can occur due to (1) due to misfitting of their rough (fold) surfaces or (2) the repelling of molecular cilia located close to the branch points of adjacent lammellae.

A critically large viscosity
The notion that impurities are a prerequisite for spherulite formation has been challenged by the observations made by Magill and others of spherulites in pure liquid environments [48, 8, 58]. Magill concludes that the fysical explanation of spherulitic growth lies in the formation under a critically large viscosity. Namely, the spherulites would only appear in pure fluids with a large viscosity (typically around 30-50 Pa·S) [48]. Gránásy et al. [28] pointed out that supercooled liquids have a glass forming nature that cause dynamic heterogenities. Dynamic heterogenities are regions within a fluid that have a much higher or lower mobility compared particles that exhibit Brownian motion. This could explain why the spherulites were observed in pure liquids. Sadlik [59] is then investigating the role of viscosity in banded-spherulitic growth, and adapts the hydrodynamic model of Tiller with a pressure term. In this study, the size of the fibrils is related to the kinetic viscosity ν by the following relation: $\delta \propto \nu^{-1/2} G^{-2}$. Although the hydrodynamic scaling factor did not hold for band spacing it still worked for the critical length. In 2016, Crist & Schultz [16] conclude in their review on polymer spherulites that a high viscosity is generally observed in inorganic and organic spherulitic growth. It's a nearly universal occurrence for spherulites to develop in viscous fluids. However, Shtukenberg et al. [65] state on the contrary that viscous growth media are not a requirement for spherulitic growth since decoupling of diffusion with viscosity was not detected for polystyrene spherulites [81]. This raises a new question for discussion; why

would decoupling of the diffusion with viscosity be essential in this context? From the Stokes-Einstein law the viscosity and the diffusion coefficient are related by:

$$D = \frac{k_B T}{6\pi a \eta}$$

where k_B is the Boltzmann factor, T is the absolute temperature, a is the hydrodynamic radius of the diffusing molecule and η the viscosity of fluid. From this relation, it becomes evident that as viscosity increases, the diffusion coefficient decreases. Consequently, an elevation in the viscosity of the freezing medium results in a deceleration of diffusion, potentially leading to a shift in the dominant growth mechanism. Furthermore, Kirkpatrick [36] already emphasized that two prerequisites for spherulitic growth are the presence of non-crystallizable components and growth rates surpassing diffusion rates, ensuring the removal of rejected components from the growing interface. This aligns with the notion that a critical viscosity level can sufficiently impede diffusion, allowing spherulites to form through a mechanism that removes non-crystalline phases from the growing front in viscous liquids.

Although the evidence suggest strongly so far that diffusion limited control is the mechanism by which spherulites grow, not everyone agrees. Heijna confirms surface kinetics to be the dominant growth mechanisms for spherulitic growth of hen egg-white lysozyme crystals, but also volume diffusion seems to play important role due to the separated liquid-liquid phase retracts from the spherulitic growth front [31]. Furthermore, noncrystallographic branching is more common for interface-controlled growth. Additionally, interface-controlled growth has been reported in spherulites grown from various polymer melts. Furthermore, Shtukenberg et al. [65] note that the kinetic coefficient of solution growth spherulites is usually small while diffusion coefficients can only vary slighty. Therefore, diffusion should be less important. However, kinetics coefficient can vary by orders of magnitude and if the kinetic coefficient is high the diffusion will be the limiting factor for growth. Since the cases that spherulites are formed in this cases are rare, Shtukenberg et al. [65] conclude that spherulites do not form under diffusion control but by interface kinetics. Therefore, they also reject the Mullins-Sekerka instability to explain noncrystallographic branching since the M-S models do not make sense for interface kinetics. Moreover it does not explain small angle orientations and all spherulite-building crystals are formed below the roughening transistion temperature.

An interplay of growth mechanisms

The interface instability problem, initially introduced by Keith and Padden, has been refined in Toda's work so that the growth rate will be controlled by secondary nucleation in the presence of a field gradient [78]. This analysis diverges significantly in its approach from the diffusion-controlled interface dynamics that form the basis of the Mullins-Sekerka (MS) model [16]. Despite the different approach, the analytical outcome of the analysis of Toda [78] was identical to the M-S model. So why is it still not clear after almost a century of research how spherulites grow? According to Xiao et al. [88], there are distinct phases during the spherulitic growth process that are governed by different growth mechanisms. While non-crystallographic branching primarily hinges on interface control, whereas surface nucleation is predominantly influenced by diffusion control. Siódmiak & Gadomski[66] confirm that it is likely that spherulitic growth can be governed by diffusion control followed by surface control. However, their paper introduces the idea that mass-convective transport conditions, rather than purely diffusive ones, play a decisive role in predicting the evolution of spherulites. This proposition is rooted in their concept of a Bi-Modal (Goldenfeld) growth mode for spherulites, wherein two phases can coexist in a synergistic manner by internal stress–strain material conditions. For single crystals, the crystalline phase must be constructed in a highly ordered matter, presumably at a higher energy cost. A competition between the crystal and amorphous emerging phases first evolves in a diffusional manner ($r \propto t^{\frac{1}{2}}$) according to the Mullins-Sekerka instability, until a mass-convection-like mode that follows $r \propto t$ takes over and proceeds with adsorbing the amorphous phase. A schematic of the two modes, Uni-Model (Mullins-Sekerka) and Bi-Modal (Goldenfeld) are presented in Fig. 2.24.

2.5.2. Growth conditions to form spherulites

So far, all studies agree that high crystallization driving force is a necessary growth condition for the formation of spherulites [65]. This is also confirmed by the extensive list of cases in which the formation of spherulites occurs by crystallization of slightly soluble salts under high supersaturation from solution

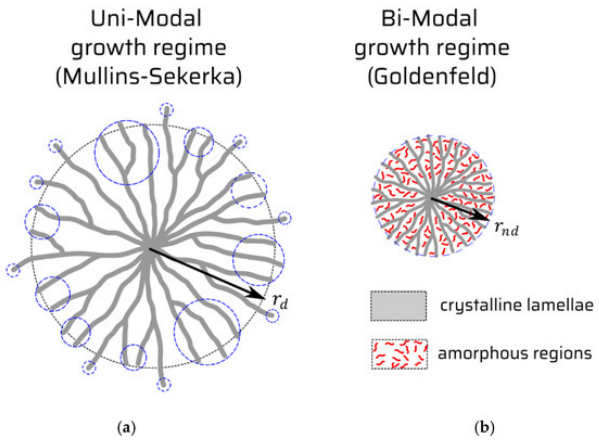

Figure 2.24: Mullins–Sekerka (M–S) type and Goldenfeld (G) type: (a) M–S, local curvatures are indicated by blue dashed circles; (b) G, mean curvature is signified by blue dashed circle [66]

or gels, while the reported cases in which spherulites were formed from highly soluble salts that grow at low supersaturations are more rare [50, 12]. Nevertheless, it is still debated whether spherulites should be associated with the metastable zone or that spherulites can be a crystal habit for specific compounds. Morse [50] argued that his extensive list of over 100 slightly soluble substances of which he could grow perfect spherulites was the proof that spherulites will continue to grow without developing plane faces instead of transform at some point to another phase [50].

Geologists have known spherulites for a long time as crystal structures in glassy igneous rocks [50]. Glassy textures form in the rocks during some volcanic eruptions when the lava is quenched so rapidly that crystallization cannot occur. Moreover, megaspherulites are believed to be formed at a temperature close to glass transition temperature (Tg) [11]. The relation between spherulitic growth and the glassy state has also been mentioned in other fields. For example, Granàsy et al.[28] point out that supercooled liquids (that are related to spherulitic growth) have a glass-forming nature. For other types of materials, it has been reported that spherulitic growth can be promoted by adding (acid-rich) polymeric additives [33]. Moreover, according to the Popcorn model by Freitas et al. [23], an amorphous intermediate can determine the polycrystallinity. However, the presence of spherulites is most abundantly studied in the field of polymer growth from the melt. Most polymers are semi-crystalline, consisting of crystalline and amorphous regions. Since glasses are formed of minerals that can crystallize and form amorphous networks, it is likely that the co-existence of a crystal and amorphous phase is a necessary condition for the growth of spherulites. This condition relates well to the almost generally accepted theory that a high viscosity is a necessary condition for spherulitic growth and the recent work of Siódmiak & Gadomski [66] that describe the transition of a Uni-Modal type to a Bi-Modal type of growth.

2.5.3. Experimental and modelling approaches

Since there is not an established method, this section will present some strategies to study the growth mechanism of spherulites and it's morphological development. First, it is discussed how to determine wether the growth is limited by diffusion or by surface kinetics. Secondly, a example of a simulation model is explained that can be used to analyse experimental observations of the morphological development of spherulites.

Determination of the growth mechanism

Directly measuring the integration or mass transfer rates at the crystal's growth interface is not always feasible, as these rates can be exceedingly small and challenging to quantify accurately. Moreover, crystallization kinetics are influenced by many factors that are challenging to isolate in experimental setups, which all add further complexity to the task of understanding crystal growth processes. Furthermore, transitions in growth behaviour may evolve, and the precise definition of where the transition is remains elusive. This section discusses methods to evaluate the ambiguous transition between diffusion-controlled growth and surface-controlled growth. To recap, surface-controlled growth in characterized by a constant growth rate G, meaning that the radius of the spherulite is growing linearly over

time. Diffusion-controlled growth is governed by the diffusion coefficient D $\propto exp(-E_A/RT)$, where E_A is the activation energy, R is the gas constant, and T is the temperature. The radius of a growing spherulite would then grow proportional to the square root of time, r $\propto \sqrt{t}$. A higher G/D ratio favours diffusion control since the diffusion rate is lower than the rate of the surface integration and, therefore, the limiting factor [65].

In solutions, this ratio can be estimated by $\xi = \Delta c_\mathrm{s}/\Delta c$ (Fig. 2.25), where $\Delta c_\mathrm{s} = c_\mathrm{s} - c_\mathrm{eq}$ is supersaturation at the growth front, $\Delta c = c - c_\mathrm{eq}$ is the supersaturation in the growth medium, c_s is the salt concentrations in the solution at the growth front [65]. ξ can vary between 0 and 1. When ξ nears zero, diffusion is rate limiting, and if ξ is 1, the rate of incorporation at the surface is limiting. Here, the growth rate is considered to be $G = \beta\,(\Delta c_\mathrm{s})^m \approx \mathrm{D}\,(\Delta c - \Delta c_\mathrm{s})\,/\delta_D$, where $\beta, \mathrm{D}, \delta_\mathrm{D}$, and m are the kinetic coefficient, diffusion coefficient, thickness of diffusion boundary layer, and order of interface reaction. If m is equal to 1, the interface kinetics is linear. However, often it varies between 1 and 2. The growth regime is primarily defined by the product $\delta_\mathrm{D}\beta/D$. The thickness of the boundary layer can be assumed to be equal to the growing crystal radius. However, the evaluation of ξ that is described above can be challenging since it requires a full understanding of the interface kinetics of the growth system.

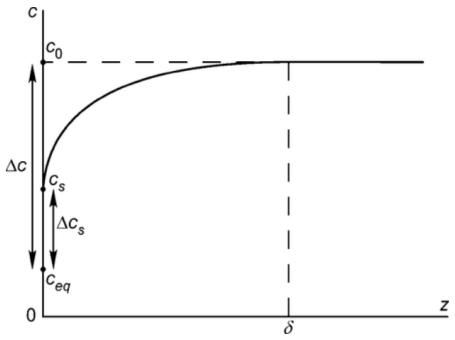

Figure 2.25: Diffusion boundary layer formed by a crystal growing from solution [65].

A more practical method is described by Shakiba et al. [63] to define if the surface or diffusive effects are more 'important' at a certain stage during crystal formation in a droplet undergoing rapid dehydration. They have adapted the Damköhler number (Da) that is usually used for a similar problem that relates the chemical reaction timescale (reaction rate) to the transport phenomena rate occurring in a system. In other words, the reaction time is governed by the timescale of the chemical source (supply) that depends on the diffusion or how fast the reaction can occur. The Damköhler number can be used to determine which of the two is the limited factor that describes the timescale of interest. The definition of the Damköhler number is given by

$$\mathrm{Da} = \frac{\text{Reaction rate}}{\text{Diffusion rate}} = \frac{\text{Diffusion time}}{\text{Reaction time}} \tag{2.16}$$

If $\mathrm{Da} \gg 1$, the reaction rate is much greater than the diffusion rate distribution, and therefore, the timescale is diffusion-limited. For $\mathrm{Da} \ll 1$ diffusion occurs much faster than the reaction, thus the reaction rate is important to describe the time scale of interest. Note that Da is associated with characteristic diffusion and reaction times, and therefore scaling is necessary. The researchers estimated the reaction time scale by considering the induction time, while the modified evaporation time scale was based on the available time for the crystal to precipitate after reaching supersaturation in the specific experimental setup. They found that at high Damköhler numbers, the surface structure of the particles appeared rough, whereas smaller Damköhler numbers resulted in relatively smoother particle surfaces. These results indicate a correlation between the Damköhler number and the surface characteristics of the formed crystals in the droplets.

Darkins et al. [18] also describe a method, based on the Damköhler number Da, to distinguish different regimes in which calcite growth kinetics are governed by reaction control and diffusion control.

By their model, the Damköhler number can be rewritten as:

$$Da = \frac{R\left(S_{\text{bulk}}\right)/\omega}{DK_{\text{sp}}^{1/2}\gamma^{-1}\left(S_{\text{bulk}}-1\right)/r} \tag{2.17}$$

In this formula, S_{bulk} is the supersaturation at the bulk, given by:

$$S = \sqrt{\frac{\left\{\text{Ca}^{2+}\right\}\left\{\text{CO}_3^{2-}\right\}}{K_{\text{sp}}}} \tag{2.18}$$

R(S_{bulk}) is the growth rate in bulk, D is the ion diffusion coefficient, K_{sp} is the solubility of calcite, γ is the activity coefficient, ω is the molar volume of calcite and r is the effective radius of a rhombohedral calcite crystal. When $\text{Da} \ll 1$, crystal growth is limited by the surface reaction, and when $Da \gg 1$, growth is limited by diffusion.

Simulating spherulitic morphologies

To enhance our understanding of spherulite growth and to facilitate comparison with experimental results, we will elucidate a straightforward simulation model proposed by Heijna et al. [31]. This model differentiates between two distinct stages:

- Stage 1: Dendritic tip with a local diffusion field around it
- Stage 2: Tip splitting by heterogeneous nucleation

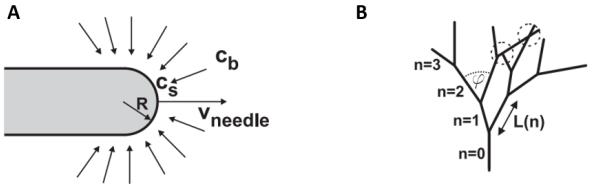

Figure 2.26: A) Model of a growing needle and its supply of material from its surroundings, B) A Cayley-like tree, showing the definition of bifurcation number n, needle length L(n) and bifurcation angle ϕ. The length of an individual needle L(n) depends on the bifurcation number with an added stochastic deviation. The dashed circles indicate a needle being blocked (left) and crossing over another needle (right). ϕ and n are estimated from experiments. [31]

The growth of spherulites begins with the formation of needle-shaped rods. In Fig. 2.26, a schematic representation by [31] is presented. On the left, the parameters of the dendritic tip are explained, while on the right, the parameters from a Cayley-like tree are illustrated, which represents the tip splitting by heterogeneous nucleation.

The concentration difference $c_b - c_s$ can be expressed for a single needle by the following equation:

$$c_b - c_s = \frac{v_{\text{needle}}\,R}{4kDV_{\text{mol}}}, \tag{2.19}$$

with c_b the bulk concentration, c_s the surface concentration, v_{needle} the growth rate of the needle, k a geometric correction factor, D the diffusion constant (found in literature), and V_{mol} the volume of one lysozyme molecule. By estimating the needle tip radius from the experiment, they found a concentration difference in the order of 400 times larger than the typical bulk concentration. This indicated that the surface concentration at the needle tips hardly drops. Therefore, surface kinetics dominates the growth process rather than mass transport. However, they derived Fick's law in spherical coordinates to consider the mass transport and approximated the spherulite as a dense, flat cylinder. As for the single needle case, an expression was found for the concentration difference $c_b - c_s$

$$c_b - c_s = \frac{\xi v_{\text{needle}}\,R}{DV_{\text{mol}}\,N_A}\ln\frac{\delta}{R}, \tag{2.20}$$

in which ξ is a density correction factor that considers the solution-filled spaces between the needles. The rate at which the surface concentration drops can be determined by substituting values for R and δ, a finite distance for c_b, taken from the experimental analysis. In a rough approximation based on experiments, they then found the surface concentration to be significantly lower than in the bulk, indicating that mass transport should not be neglected. For the tip splitting of the needle, it could be assumed that the top faces have a rough growth mechanism and are split by heterogeneous nucleation. The growth rate of the needles is proportional to the supersaturation, and the nucleation rate depends on the driving force by the following relation:

$$J \propto e^{-f\gamma^3/\Delta\mu^2 kT} \tag{2.21}$$

with γ the edge free energy, k Boltzmann's constant and T the temperature. Further, $f = \frac{16K}{3}\pi\Omega^2$ in which Ω is the volume of a growth unit, and K is a constant depending on the equilibrium shape of the heterogeneous nucleus. To simulate the morphology with the Cayley-like tip splitting, the number of times the needles have split (n) and the bifurcation angle ϕ are estimated from experiments (Fig. 2.27). ϕ can be measured from images, and an estimation for n is given by α_{final}/ϕ.

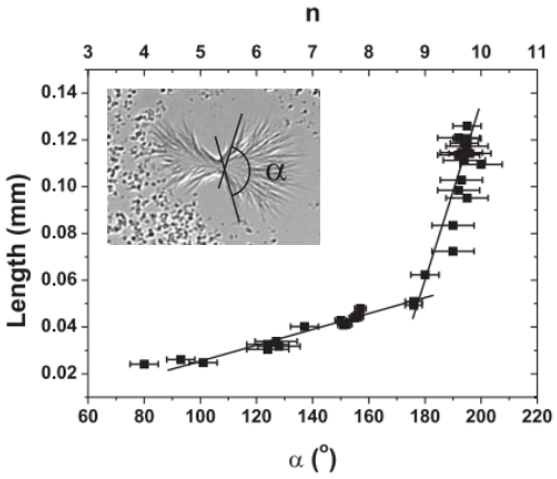

Figure 2.27: The angle, α, of one side of the spherulite, versus the length of the side and n, which indicates the number of tip splittings. The linear fits are given relations to the simulated morphology [31]

We have explained a simplistic model to simulate spherulitic morphologies. However, phase field modelling is the most appropriate and used strategy for simulating spherulitic growth. The basis of phase-field modelling for morphological predictions is well described by Robert Sekerka in the Theory of Crystal Growth Morphology [61]. A detailed explanation of phase-field modelling is beyond the scope of this theoretical background. Nevertheless, the basis of the phase field model is that a diffuse interface replaces a sharp interface. A continuous variable ϕ(the phase) that can equal 0 in the solid and 1 in the liquid is introduced. In the thin layer that corresponds to the diffuse interface, the phase can vary between 0 and 1. The phase is governed in time by a partial differential equation, which depends on relevant variables such as temperature (for energy transport) and composition (for solute transport). Furthermore, the diffuse interface has excess energy related to the surface tension, by which a curvature will give rise to capillary.

Other models related to the prediction of crystal morphologies come from the Bravais-Friedel-Donnay-Harker (BFDH) method, Density Function Theory (DFT), and molecular dynamics modelling.

3

Experimental method

3.1. Preparation of sulfate salt mixtures

Sodium sulfate (Na_2SO_4) has anhydrous (known as thenardite) and hydrated (hepta- and decahydrates) crystalline polymorphs. The heptahydrate is rarely observed and only in laboratory experiments. At room temperature (21 $\pm$ 0.5 °C), the decahydrate (known as mirabilite) is the more stable hydrated form of sodium sulfate in the experimental conditions (see phase diagram in the Supplementary). However, if the hydrated crystals are left in contact with air, they will transform into thenardite. The salt mixtures are prepared by dissolving thenardite (Na_2SO_4) and either ironsulfate heptahydrate ($FeSO_4 \cdot 7H_2O$) or magnesiumsulfate heptahydrate ($MgSO_4 \cdot 7H_2O$) in Millipore water ($\rho \sim 18.2\mathrm{M\Omega \cdot cm}$). The amount of water in which the thenardite is dissolved is determined such that the molal concentration in the solution is approximately 0.7 times the solubility of mirabilite ($Na_2SO_4 \cdot 10H_2O$). The amount of iron sulfate heptahydrate ($FeSO_4 \cdot 7H_2O$) or magnesium sulfate heptahydrate ($MgSO_4 \cdot H_2O$) is calculated based on the desired molar fraction, Y. The molar fraction of $FeSO_4$ is given by equation (4.3) and the molar fraction of $MgSO_4$ by equation (4.4). Y=0 corresponds to a pure Na_2SO_4 solution and 1 corresponding to a pure $FeSO_4$ or $MgSO_4$ solution. Depending on the amount of $FeSO_4$ or $MgSO_4$, extra water is added based on the solubility of the salt so that the salt solution is undersaturated before evaporation. The salts are weighted with a 0.05 g precision and are dissolved for at least 30 minutes while stirring (300-500 rpm).

3.2. Nucleation and growth observations by Optical Microscopy

The salt mixtures are prepared according to the method of preparation described above. We performed evaporation experiments on salt mixture droplets with a volume of 1 $\pm$ 0,2 μL. With a micropipette a droplet is extracted from the bulk solution and placed on a glass slide $\left(k_s = 1.0 \pm 0.2\mathrm{Wm^{-1}\ K^{-1}}\right)$ clean with ethanol and Millipore water. The experiments are performed at constant room temperature T = 20 $\pm$ 1 °C. The relative humidity is, if necessary, adjusted by using a (mini) climate chamber attached to RH controller(details are described in [62]). With a Leica Optimal Microscope attached to a computer with Pixellink software the crystallization within the droplets during the drying process is recorded with a frame rate of 0.5 fps. From the recorded frames, the crystallization kinetics could be characterized. The growth rate is determined by measuring the length of the spherulites in time. While the droplets dry, the concentration of salt ions will increase until a critical supersaturation is achieved and instantaneous crystallization occurs. Additionally, evaporative experiments of small volumes ($\leq 1\mu$L) are performed in a square microcapillary of 0.5x0.5 mm, which is slightly lifted by placing a tape on the glass slide to avoid creeping by contact at the opening. The glass slide with capillary is placed in the mini climate chamber to determine the supersaturation on the onset of crystallization under controlled evaporation (RH=40%, RH= 50%, and RH=70%). The volume difference in time (V_i - V_t) is followed by measuring the displacement of the two menisci of the salt solution that is trapped in the capillary (Fig.4) by the CCD camera that is connected to the optical microscope. For each experiment, the concentration is determined from the volume difference between the initial volume (V_i) and the volume at which the spherulites nucleate (V_p). The supersaturation at the moment of precipitation is defined as $S = C_p/C^*$,

which is the ratio between the molal concentration at the moment of precipitation $C_p = \frac{C_i * V_p}{V_i}$ and the equilibrium concentration (C*).

3.3. Viscosity measurements

By comparing the rheological measurements of solutions with the same amount of salts (Y_{Mg}=0.2) but with a reduced amount of water, we could measure the viscosity as a function of the supersaturation. The initial solution is prepared with 0.89 g $MgSO_4 \cdot 7H_2O$, 3.85 g Na_2SO_4 and 21 g H_2O. Between the other solutions, the amount of water $m[H_2O]$ is reduced to 0.48 - 0.8 times the initial mass of water m_i [H_2O]. $\sim$ 500 μL of the solution is placed with a pipette between the cone-plate geometry (max.gap=0.053 nm, diameter=50 nm) of an Anton Paar Modular Compact rheometer (MCR300). The rheometer has a Peltier element by which the temperature is first increased to 30 °C so that the over-saturated solutions completely dissolve. Then, the temperature is brought down to 20 °C to measure the increase in viscosity. The viscosity is measured per second from a continuous shear (dγ/dt = 900 1/s) until it reaches a plateau.

3.4. Structural and chemical characterization

Raman Confocal Microspectroscopy is performed with a WITec, Alpha 300 R microscope coupled to a CMOS camera (Andor, Newton EMCCD, DU970P−BVF−355). The wavelength of the laser is 532 nm with a diffraction grating of 600 mm^{-1}. While Raman spectra provide an extensive chemical, physical, and structural insight into a local point of interest in the sample, confocal microscopy enables high-resolution volume analysis within the sample in both the lateral (XY) and axial (Z) axes. Thus, the technique brings high-resolution chemical imaging of the material at the microscale.

Scanning Electron Microscopy is performed using an FEI Verios 460, equipped with an Everhart-Thornley detector (ETD) and a circular backscatter detector (CBS), to investigate the structure and surface of the spherulites from nano- to microscale. Spherulite-containing samples were prepared with an 80 nm thick coating of gold particles. The SEM is used with an accelerating voltage of 10 kV and a current of 100 pA to acquire the high-resolution images.

4

Results

4.1. Thermodynamic equilibria of phases in aqueous binary sulfate salt mixtures

We performed evaporation experiments involving two types of salt mixtures containing bivalent ions: (1) an aqueous mixture of $Na_2SO_4 - FeSO_4$ and (2) an aqueous mixture of $Na_2SO_4 - MgSO_4$. To the best of our knowledge, the phase diagrams of these binary systems have not been documented in existing literature. However, obtaining accurate values for the thermodynamic equilibria of the precipitating phases is essential for comprehending the growth conditions under which precipitates crystallize. Therefore, the phase diagrams for these specific salt combinations must be derived.

The solubility phase diagram of pure sodium sulfate in water has been reported before by Steiger et al.[68] and is presented in Fig. 4.1(A). The solubility phase diagram of the pure system includes the hydrous phases of sodium sulfate; the decahydrate $Na_2SO_4 \cdot 10H_2O$ that is known as mirabilite (1) and the metastable heptahydrate $Na_2SO_4 \cdot 7H_2O$ (4). At the top half of the graph, the lines of anhydrous $Na_2SO_4(V)$ (2), also known as thenardite, lies below its metastable form $Na_2SO_4(III)$ (3). Furthermore, the phase diagram presents the freezing (5) and boiling (6) temperatures. The solubilities of sodium sulfate phases under our experimental conditions (T=20.5 °C) are depicted in the phase diagram through red dotted arrows. Detailed thermodynamic properties for iron sulfate and magnesium sulfate in water can be accessed in the Supplementary section. Additionally, the Supplementary provides a comprehensive list of solubilities for all compounds in pure systems at T=20.5 °C.

The symbols in the $Na_2SO_4 - H_2O$ phase diagram are experimental data that Steiger et al. [68] collected from the literature. Except for the metastable $Na_2SO_4(III)$, the experimental data validates the modelled solubility lines. The computed lines are calculated by a molality-based model that Steiger et al.[69] developed. The model includes ion interactions to calculate the phase equilibria in multicomponent salt systems. For a given salt of composition $M_{\nu_M}X_{\nu_X} \cdot \nu_0 \mathrm{H_2O}$, consisting of ν_M positive ions M of charge z_M, ν_X negative ions X of charge z_X and ν_0 molecules of water, the equilibrium constant K_{MX} of the dissolution reaction is expressed as follows:

$$\ln K_{MX} = \nu_M \ln m_M + \nu_X \ln m_X + \nu_M \ln \gamma_M + \nu_X \ln \gamma_X + \nu_0 \ln a_{\mathrm{w}} \tag{4.1}$$

where m_M, m_X, γ_M and γ_X represent the molalities and activity coefficients of the cations and anions, respectively. The water activity a_{w} is defined as:

$$\ln a_{\mathrm{w}} = -\phi M_{\mathrm{w}} \sum_i m_i \tag{4.2}$$

where ϕ is the osmotic coefficient and $M_{\mathrm{W}} = 1.801528 \times 10^{-2}\ \mathrm{kg\ mol^{-1}}$ is the molar mass of water. To calculate the activity and osmotic coefficients that are needed to determine the thermodynamic solubility products of solid phases, the model employs the Pitzer equations [56]. These equations facilitate the calculation of excess Gibbs energy in electrolyte solutions. Subsequently, the activity and osmotic coefficients are derived from the Gibbs free energy equation as a function of composition and temperature. For a more in-depth understanding of the model, please refer to the comprehensive explanation

and equations provided in the publication of Steiger et al.[69].

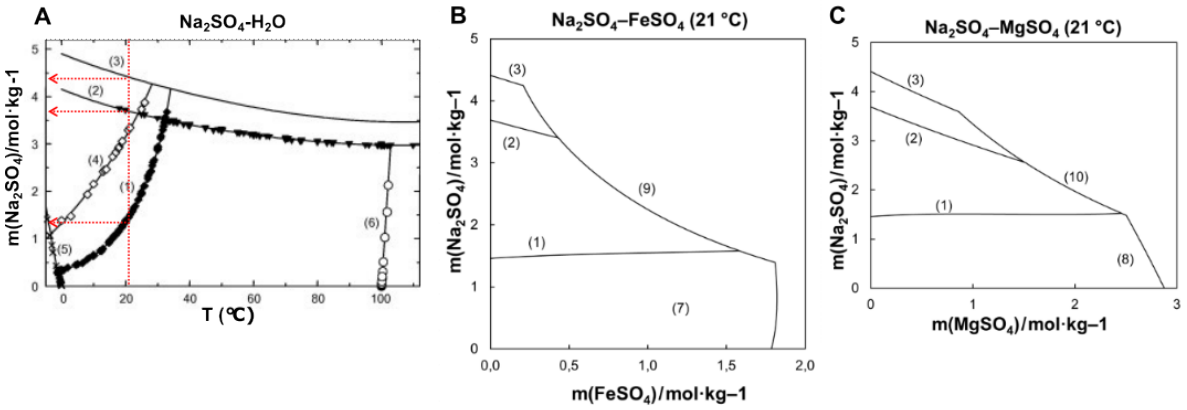

Figure 4.1: **Thermodynamic equilibria of phases in aqueous sulfate solutions**. The solubilities of sodium sulfate phases; (1) Na2SO4·10H2O (mirabilite), (2) Na2SO4(V) (thenardite), (3) Na2SO4(III), (4) Na2SO4·7H2O, and (5) freezing temperatures and (6) boiling temperatures, and at roomtemperature stable iron and magnesium phases; (7) FeSO4·7H2O (melanterite), (8) MgSO4·7H2O (Epsomite), and the double salts; (9) Na2Fe(SO4)2·4H2O and (10) Na2Mg(SO4)2·4H2O (bloedite), are presented in (A) The solubility phase diagram of the Na2SO4–H2O system [68], (B) in the binary phase diagram of the $Na_2SO_4 - FeSO_4$ system at T= 21 °C, and (C) and in the binary phase diagram of the $Na_2SO_4 - MgSO_4$ system at T= 21 °C. The lines represent the results from the Pitzer Model of Steiger et al. [69] and the symbols represent experimental data that they collected from the literature.

The solubilities of phases in the two binary systems are computed at T=21 °C using the model proposed by Steiger et al. [69]. The results are presented in the binary phase diagrams in Fig. 4.1(B) and Fig. 4.1(C). In the graph of the $Na_2SO_4 - FeSO_4$ system, the lines intersect the Y axis at the solubilities of the sodium sulfate phases (1,2,3) in a pure $Na_2SO_4 - H_2O$ system that corresponds to the values indicated by the red arrows in 4.1(A). In the graph in 4.1(B), the X axis is intersected by the line from the iron sulfate phase that is stable at room temperature; $FeSO_4 \cdot 7H_2O$ (7), which is also known as melanterite, at its solubility in a $FeSO_4 - H_2O$ system. Similarly, the X axis of the graph in 4.1(B) intersects $MgSO_4 \cdot 7H_2O$ (Epsomite) (8) at its solubility. The lines of the previously mentioned phases are cut off by the solubility lines of the double salts (9) $Na_2Fe(SO_4)_2 \cdot 4H_2O$ and (10) $Na_2Mg(SO_4)_2 \cdot 4H_2O$ (bloedite). We can compare the solubilities of the phases in the binary salt mixtures with the solubilities in a pure sodium sulfate system by starting at the Y axis that represents the pure $Na_2SO_4 - H_2O$ system at T=20.5 °C (red dotted line in Fig. 4.1(A)). By moving to the right where m($FeSO_4$) ~ 0.25, meaning that the molar fraction of the bivalent ion in the solution increases, the solubility lines of thenardite (2) and phase III (3) go slightly down, while the solubility line of mirabilite (1) goes slightly up. Our results that are presented in the binary diagrams provide the information to determine the solubility, depending on the molar fraction of $FeSO_4$ or $MgSO_4$ in the solution. We can define the molar fraction of $FeSO_4$ in the sulfate solutions as

$$Y_{Fe} = \frac{n_{FeSO_4}}{n_{FeSO_4} + n_{Na_2SO_4}} \tag{4.3}$$

and similarly of $MgSO_4$ as

$$Y_{Mg} = \frac{n_{MgSO_4}}{n_{MgSO_4} + n_{Na_2SO_4}} \tag{4.4}$$

where n_{FeSO_4}, n_{MgSO_4} and $n_{Na_2SO_4}$ are the molar masses of iron sulfate (heptahydrate), magnesium sulfate (heptahydrate) and sodium sulfate (thenardite), that are dissolved in the aqueous sulfate solution.

4.2. Morphological transition of sodium sulfate spherulites as a function of the bivalent ion concentration

The evaporation experiments entail the variation of Y between 0 and 1, with Y=0 indicating a pure Na_2SO_4 solution and 1 corresponding to a pure $FeSO_4$ or $MgSO_4$ solution, to study the effect of bivalent

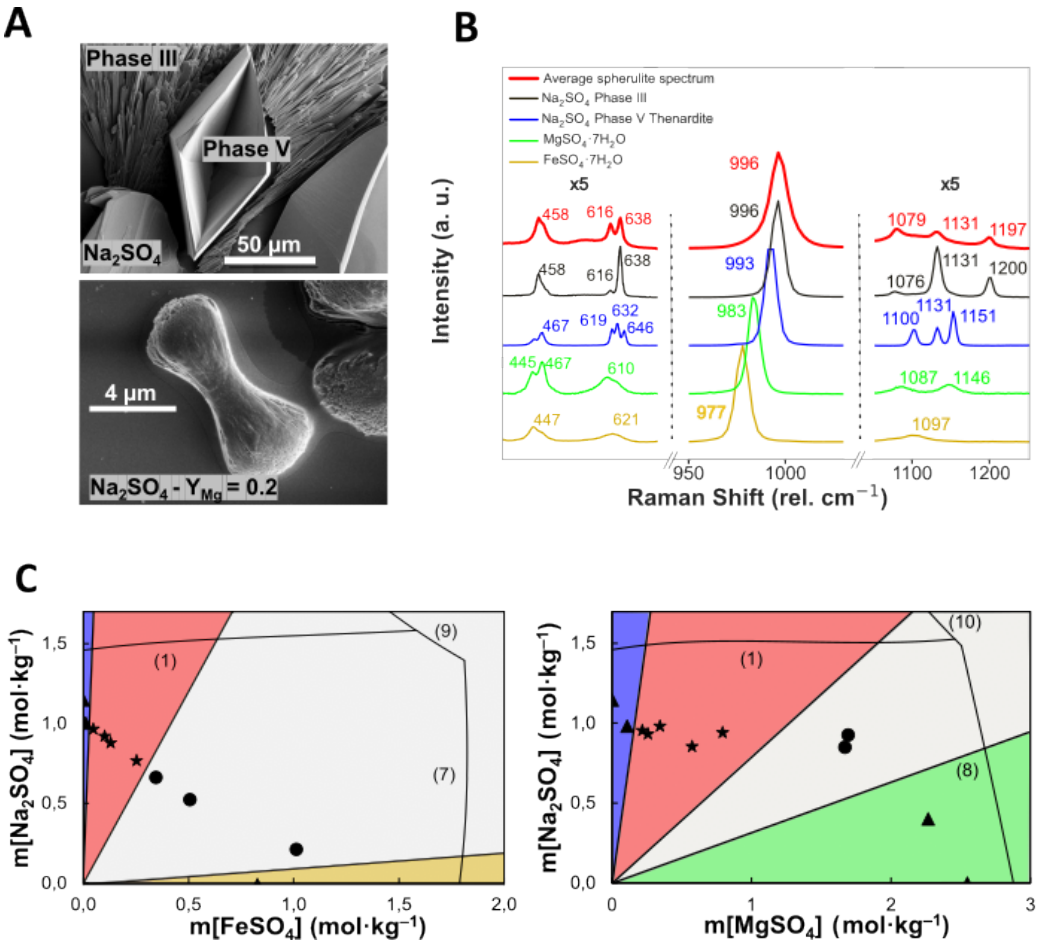

Figure 4.2: **Effect of bivalent ions on the crystallization from sulfate salt mixtures** (**A**) SEM images of crystals. Top: Stable rhombohedral thenardite and needle-like metastable phase III from pure Na_2SO_4 solution [reproduced with permission from [10]]. Bottom: (Premature) Na_2SO_4 spherulite crystallized from sulfate mixture (Y_{Mg}=0.2). Between spherulites there is another phase (red arrow) (**B**) Average Raman spectra of 7 spherulites (red) and Raman spectra of Na_2SO_4 phase III (black), Na_2SO_4 phase V (blue), $MgSO_4 \cdot 7H_2O$ (green), $FeSO_4 \cdot 7H_2O$ (yellow). Left and right regions are 5x magnified. (**C**) Morphodroms of Na_2SO_4 - $FeSO_4$ system (left) and Na_2SO_4 - $MgSO_4$ (right), including thermodynamic equilibria from Fig. 4.1. Different crystalline structures, presented as triangles (polyhedral crystals) and stars (spherulites), will precipitate in the salt mixtures depending on the molar fraction Y. Delayed crystallization by an amorphous state is denoted with dots. Coloured areas, similar to colour-coded as (C), indicate regions between Y values (black lines) where the precipitates are expected.

ions on the crystal morphology. Hereafter, the aqueous $Na_2SO_4 - FeSO_4$ and $Na_2SO_4 - MgSO_4$ solutions are referred to as the Fe or the Mg solution, accompanied by its molar fraction Y. 1 μL droplets of the prepared unsaturated salt mixtures were left to dry on a cleaned glass slide and observed under the optical microscope. As a droplet is left to dry, the water evaporates, and the concentration increases until, at some point, salt crystals nucleate. The top SEM image in Fig. 4.2(A) shows the morphologies of anhydrous phases expected after drying a pure Na_2SO_4 solution. The needle-shaped crystals on the side are the metastable phase III that transforms into the stable phase V (rhombohedral crystal in the middle). In this experiment, the evaporation is too fast for all phase III needles to transform into phase V. Surprisingly, repeating the same experiments with a salt mixture containing bivalent ions (Y_{Mg}=0.2) results in the formation of spherulites of anhydrous Na_2SO_4 instead of the needle or rhombohedral-shaped crystals. With Raman spectroscopy, the average spectrum of 7 spherulites is compared with the spectra of Na_2SO_4 phases and the spectra of $FeSO_4 \cdot 7H_2O$ and $MgSO_4 \cdot 7H_2O$ to determine the nature of the spherulites precipitate. In Fig. 4.2(B) the overlapping Raman peaks (458, 616, 638, 996, 1076-1079, 1131, 1197-1200 cm^{-1}) of the average spectrum (red) and phase III (black), reveal that the spherulites consist of crystals from the needle-shaped phase III of sodium sulfate.

The effect of the bivalent ions is investigated by varying the molar ratio Y in the two salt mixtures. During the experiments, the temperature is kept constant (20.5 °$C \pm$ 1%). The relative humidity did not

vary significantly in the experiments with the Fe solution (50-60 $\pm$ 2%) and varied between 40-60 $\pm$ 2% in the experiments with the Mg solution. The experiments resulted in three main different outcomes by which they are classified in the morphodroms in Fig. 4.2(C); (i) If spherulites were present during the crystallization process, they were classified as such, even if they became imperceptible after the completion of the drying process. (ii) Instances where crystallization did not involve spherulites but instead led to the precipitation of regular polyhedral-like crystals were categorized as 'non-spherulitic crystals' (e.g. rhombohedra for Na_2SO_4). (iii) The third scenario occurred when no crystallization occurred within the experimental timeframe (≤30 min). In these cases, the liquid droplets stopped evaporating and surprisingly transformed into a gel state. Subsequently, when these gel droplets were allowed to dry over a longer period, crystallization involving spherulite growth could still occur later, typically occurring approximately after a day; however, the quantification of this phenomenon will be the subject of another study. The experimental results by varying Y_{Fe} in the Fe solution are presented in the left phase diagram in Fig. 4.2(C). The dashed line extends from the solubility of pure sodium sulfate on the Y-axis to the solubility of pure $FeSO_4 \cdot 7H_2O$ at the X-axis at experimental conditions ($T = 20.5 \pm 1$ °C). We can describe the morphology of precipitating crystals versus the initial concentrations in a morphodrom with domains of occurrence for each category. The domains are separated by borders that are defined by

$$m[Na_2SO4] = \frac{(1-Y)}{Y}(m[FeSO_4] \wedge m[MgSO_4]), \tag{4.5}$$

derived from Eq. (1). The borders are drawn in the middle between the two closest data points that define a transition from one dominant morphology to another. For the Fe solution, the area of spherulites (black stars) is defined by $0.03 < Y_{Fe} < 0.29$. By following the dashed line downwards (meaning that Y_{Fe} increases), the solidification to a gel state (black dots) becomes more dominant and delays the crystallization. The area in which only the gel state is observed in the time intervals of our study is between $0.29 < Y_{Fe} < 0.91$. When Y_{Fe} is close to 1, $FeSO_4 \cdot 7H_2O$ crystals are crystallizing from the evaporating droplet. Similarly, in the phase diagram of the Mg salt mixtures on the right. The same transitions are observed by increasing Y_{Mg}: from regular polyhedral Na_2SO_4 crystals to spherulites, from spherulites to the gel state, and from the gel state to $MgSO_4$ crystals. However, there are discrepancies in molar fractions that define the boundaries in the morphodrom. For the Mg solution, the area of spherulites is shifted slightly to $0.18 < Y_{Mg} < 0.46$, while the range of the gel state ($0.46 < Y_{Mg} < 0.76$) is more narrow compared to the Fe phase diagram. To further investigate the growth of the spherulites, we chose to proceed with $Y_{Fe} = 0.12$ and $Y_{Mg} = 0.2$ in the upcoming experiments detailed in this paper. These compositions were consistently effective in producing spherulites within a practical timeframe.

4.3. Effect of the evaporation rate on final crystal morphology

The evaporation rate and the initial volume are known to be important parameters in the morphological evolution of crystals. For a given volume, we investigate the effect of the evaporation rate on the growth of the spherulites in the evaporating droplets by varying the relative humidity between 30%-80% with a microclimate chamber. The fraction of bivalent ions (Y) is taken constant ($Y_{Fe} = 0.12$ and $Y_{Mg} = 0.2$). Spherulitic growth is observed in all experiments where the RH is between 30%-60%. However, depending on the evaporation rate, the final morphology of the polycrystalline structures could vary. In Fig. 4.3(A) and Fig. 4.3(B), optical microscopy images reveal the final morphologies from the edge to the centre of the droplets for RH between 30%-60% after droplets of the Fe solution and Mg solution have evaporated. After drying at a high evaporation rate (RH=30%), the precipitate consists mainly of a large amount of premature small spherulites (red square). Fewer but larger fully developed spherulites in the bulk can be observed at higher RH. Similar to the dried droplets of the Mg solution, the spherulites appear comparatively smaller along the periphery of the droplet. Moreover, when the evaporation is slow enough in the centre bulk region of the droplet of Mg solution, faceted crystals grow from the spherulites. In contrast, the spherulites in droplets of the Fe solution remain in their spherical shape. If the relative humidity is high enough, the facets can even start to crack into tiny pieces (Suppl. Video 1). Although it is unclear why the facets are not observed in the Fe solution, it might be related to the presence of oxyhydroxides that can act as nucleation sites. With this type of heterogeneous nucleation, there are more points to nucleate from. Therefore, the induction time will be relatively shorter since the oxyhydroxides provide more surface that can incorporate ions. If the induction time is relatively shorter, the overall crystallization process is shorter, and the spherulites

will 'freeze' into their shape before growth can proceed further. The overall morphological evolution that we observed from premature spherulites towards fully-developed (round) spherulites and finally towards more stable forms is presented in the schematic in Fig. 4.3(C). We generally observe in all experiments that when the evaporation rate is higher and the induction time is shorter, the spherulite's growth will stop at an earlier stage in this morphological evolution. When the evaporation is slower, and the induction time longer, enough solute is still around to grow into a fully-developed spherulite and evolve towards more faceted polyaggregated crystals. Surprisingly, the Raman spectrum of the faceted crystals is not phase V sodium sulfate but an unknown phase that requires further research.

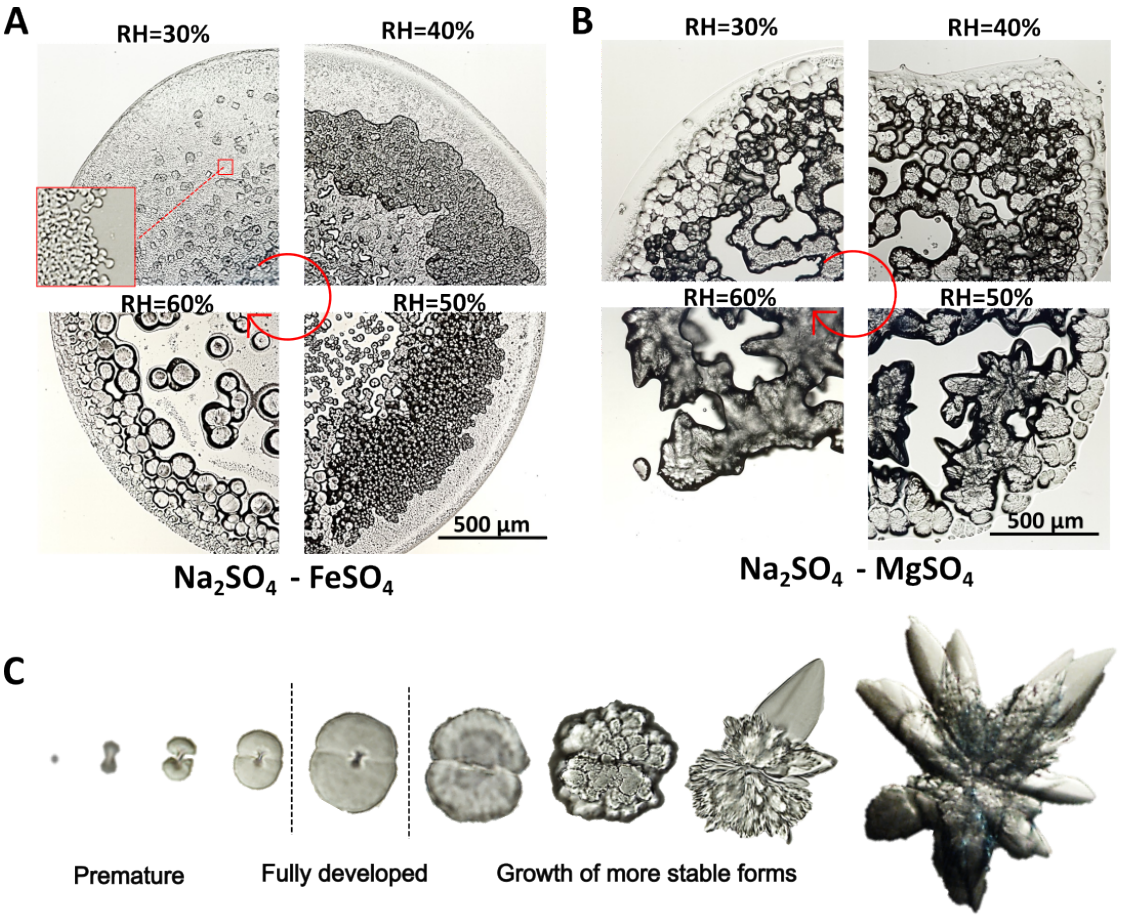

Figure 4.3: **Effect of evaporation rate and morphological evolution** (**A**) Experimental results of varying the relative humidity for the Fe solution ($Y_{Fe} = 0.12$). The RH increases with a clockwise rotation. (**B**) Similarly, as in (A), but with the Mg solution ($Y_{Mg} = 0.2$). (**C**) Morphological evolution from a premature spherulite to a fully-developed spherulite and finally a faceted phase growing on top of the spherulite.

4.4. SEM imaging revealing the self-organized structure of the spherulites

The electron microscopy pictures in Fig. 4.4 give detailed information on the level of self-organization within the spherulites. In the zoom-in of the outside of the spherulite (Fig. 4.4(A)), we observe that the spherulite consists of self-organized polycrystalline material with needles that are $\sim 2\ \mu$m in length. However, the zoom-in of the centre part of the spherulite (Fig. 4.4(A)) reveals an assembly of nanocrystals. The nanosized aggregated crystals ($\sim$ 10-100 nm) are aligned in the growth direction and perpendicular to the centre eyes of the spherulite. In Fig. 4.4(B), electron microscopy images of single spherulites portray the morphological evolution that is described before in Fig. 4.3(C), from premature spherulite (top) to fully-developed spherulite (bottom).

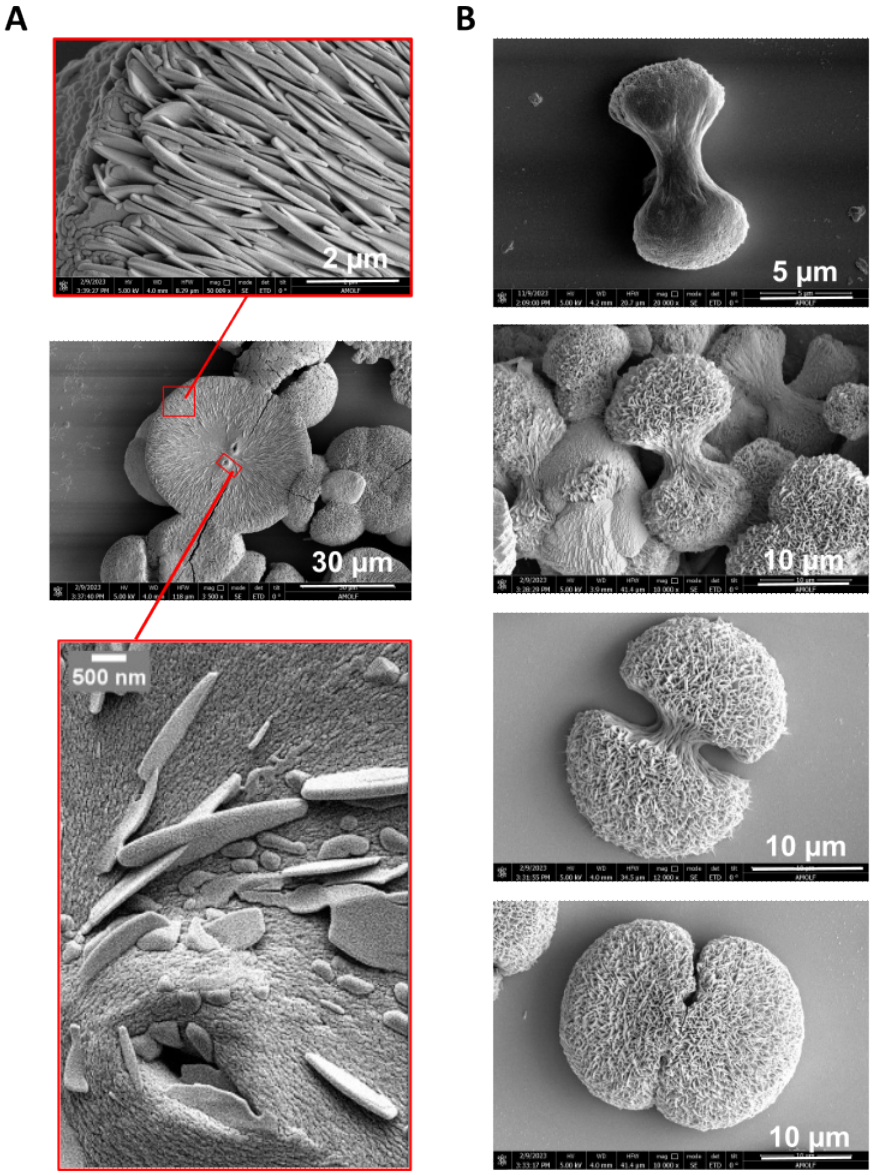

Figure 4.4: **The self-organized structure of the spherulites (from nm to μm) revealed by electron microscopy**. (**A**) Zoom-in of the centre and outside of a spherulite. (**B**) Evolution of a spherulite from premature (top) to fully-developed spherulite (bottom).

4.5. Observation of pre-nucleation clusters

While scanning electron microscopy unveiled the fascinating self-assembly of spherulites at the nanoscale, the initiation mechanism of spherulitic growth remains elusive. Although our microscopic capabilities do not facilitate dynamic observations of the initial nucleation stage, we did observe clusters within the droplets preceding the growth of spherulites. The optical microscopy images in Fig.4.5, reveal how a spherulite grows from one of the ~ 1 μm-sized zones (red arrow). In similar magnitudes of confinement, Wang et al. observed amorphous calcium sulfate to agglomerate and recrystallize in nanocrystals [83]. Moreover, a two-step nucleation mechanism model for polycrystalline nanocrystals involving confinement by an amorphous phase has been proposed recently by Freitas et al.[23]. We believe that the

formation of the gel network induces the observed pre-nucleation clusters, which are highly concentrated with ions. If spherulites nucleate by two-step nucleation, this would explain why the spherulites grow in large numbers and are dispersed over the evaporated droplet.

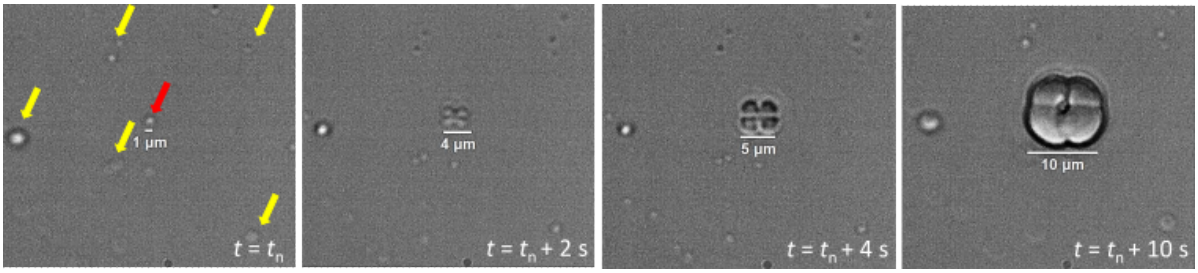

Figure 4.5: **OM observations suggest a two-step nucleation pathway through concentrated liquid droplets** The yellow and red arrows highlight the 1 μm-sized pre-nucleation clusters in an OM image at the moment of nucleation. The dot that is highlighted by the red arrow transforms into two interlocked premature spherulites that fuse into a spherulite of 10 micrometres while they grow in a time range of 10 seconds.

4.6. The effect of confinement and the growth mechanism

As mentioned before, the growth that leads to this morphological evolution can be controlled by the kinetics of incorporation of atoms on the crystal surface or by the rate at which the atoms travel towards the surface by diffusion. We investigate the growth mechanism by measuring the temporal evolution of the size of the spherulites from both salt mixtures at RH=50%. In Fig. 4.6(A), 5 spherulites of the Mg solution are displayed, of which the growth is measured upon their precipitation. Here, the spherulites are numbered based on a rough estimation of their relative distance to the edge of the droplet, with spherulite 1 being the closest to the edge. The length L (μm) of the 5 spherulites is plotted against the square root of time in Fig. 4.6(B). We find that L (μm) $\sim \Delta \sqrt{t}$, with $3.9 \leq \Delta \leq 9.6$, meaning that their growth is limited by diffusion. Remarkably, the growth rate of spherulites near the droplet's periphery is consistently lower than those within the bulk. For morphological control, we should understand what is causing this difference in growth rate and why this leads to their distinct spherical morphology when compared to the cauliflower-shaped spherulites that develop farther from the edge. The locally non-uniform evaporation rate (illustrated in Fig. 4.6(C)) elucidates the morphological differences corresponding to spherulites at lower relative humidity, as presented previously in Fig. 4.3. However, it does not directly account for the growth delay at the droplet's edge. On hydrophilic surfaces, such as the glass slides that were used here, the initial contact angles are reduced, leading to a confinement effect on the edge of the droplet [62]. By the effect of confinement and the high evaporation rate at the three-phase contact line, there is a reduced solvent availability at the edge of the droplet. However, initial observations reveal the pre-nucleation clusters at first at the contact line, where spherulitic growth commences. Notably, by advection towards the contact line, the concentration of ions is higher, and we observe that the gel state, which slows down the growth, is more present in this region than in the bulk. Influenced by these factors, the spherulites in this experiment (RH=50%) manifest a distinctive growth pattern, forming perfectly round shapes at the droplet's edges. Within the bulk, where more solvent is available, the consumption of ions by spherulitic crystals reaches a point where the reaction rate can closely match the diffusion rate and a morphological transition can be observed. Additionally, we observed especially at the edges that the spherulites are deformable (Fig. 4.6(A)), similar to mirabilite crystals that are in contact with their saturated salt solution at their deliquescence point [85]. The deformability makes the spherulites more susceptible to suppression by the confinement, which explains why the spherulites are flattened on the edge and not in the bulk.

The measured growth of spherulites in the Fe solution at RH=50% can be found in the Supplementary. The results are in agreement with the temporal evolution of the spherulites in the Mg solution. The average growth of the spherulites in the Fe solution has the same slope (3.9) as the lower limit of the growth of spherulites in Mg solution, and their morphology is comparable to the spherulites in Fig. 4.6 that are closer to the edge.

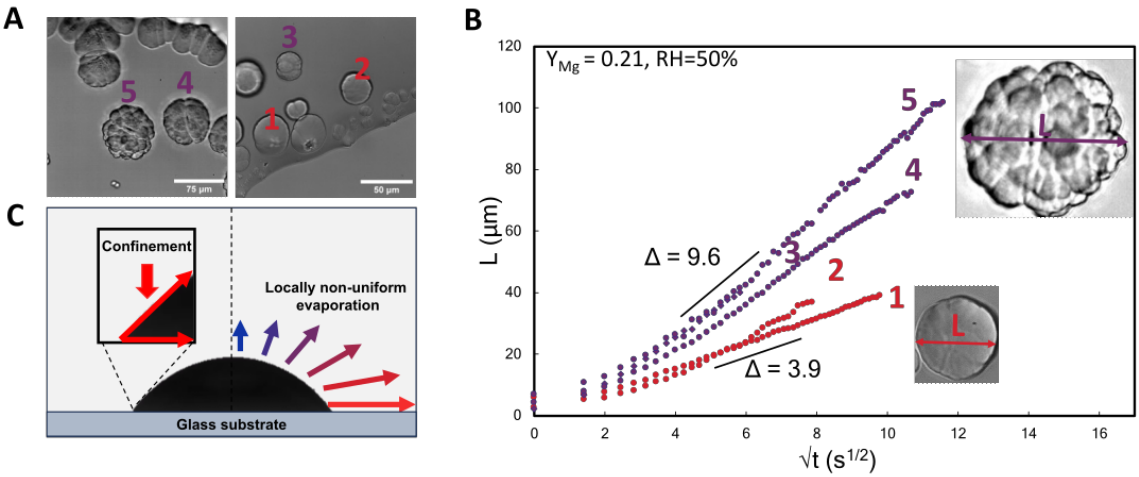

Figure 4.6: **The effect of confinement and the growth rate of spherulites of Na_2SO_4 at RH=50%** (**A**) Measured spherulites and their location relative to the edge; spherulite 1 and 2 close to the contact line and 3, 4 and 5 towards the centre of the droplet (**B**) Length L, as a function of the square root of time. The linear trend indicates that the growth of the spherulites is controlled by diffusion. The further away from the edge of the droplet (spherulite 5), the higher the slope of the growth. (**C**) Schematic of the droplet evaporating. On the left, the effect of confinement on the spherulites that form on the edge is illustrated and on the right, the non-uniform evaporation rate where the evaporation is highest at the three-phase contact line (red) and lowest at the top (blue).

4.7. Determination of the supersaturation by evaporation in micro-capillaries

According to Sunagawa's theory, spherulitic growth requires a high supersaturation. However, experimental quantifications of the supersaturation at the moment of nucleation can, depending on the crystallization method, be challenging and therefore rare [65, 44]. This can be achieved for evaporative crystallisation by evaporating the salt solution in a microcapillary under controlled conditions. Following the method described by Desarnaud et al.[19], the volume of the solution is calculated from the dimensions of the capillary and the distance between the two menisci, which evolves with the evaporation in time. The concentration at the moment of precipitation is determined by the difference between the initial volume (V_0) and the volume at the moment the system starts to nucleate (V_n). In this study, small volumes ($\sim$ 0.1 - 1 μL) of the unsaturated Mg solution ($Y_{Mg} = 0.2$) are left to evaporate in a square microcapillary of 0.5 x 0.5 mm until nucleation and growth of spherulites is initiated (illustration on the left of Fig.4.7A). The fraction of remaining mass is given by m/m_i and plotted against the time, t (min), in the middle of Fig.4.7A. In this experiment, the relative humidity is controlled with a microchamber and varied between 40%-70%. Interestingly, spherulites precipitated in all experiments at the same fraction of remaining solution $< m/m_i > (t_n) = 0.27 \pm 0.02$, regardless of the varying RH or initial volume. On average, the fraction of water that is removed by the evaporation leading to a higher concentration is therefore $< (m_i - m)/m_i > (t_n) = 0.73$. Based on the initial concentration of the salt solution and the removed water, the increasing concentration can be followed in time. On the right of Fig. 4.7(A), the molal concentration in time of the initially added Na_2SO_4 is plotted for every experiment. The average molal concentration at the onset of crystallization is $< C(t_n) >= 4.76 \pm 0.32$ (mol/kg) (dotted line). Using the relation in equation (3), we can plot a line in the previously found Na_2SO_4- $MgSO_4$ phase diagram that presents the Mg solution (Y_{Mg}=0.2), see dashed line in Fig. 4.7(B). When a droplet of the $Y_{mg} = 0.2$ solution is evaporating, the concentration increases, which corresponds to moving away from the origin along the dashed line. At some point, the line intersects the line of phase III at m(Na_2SO_4) = 3.5 (mol/kg), representing the solubility C* of phase III in the $Y_{mg} = 0.2$ solution. Together with the average molal concentration at the onset of crystallization, the average supersaturation is found to be $< S >_{Mg} = < C(t_n) > / C^*_{III}$ = 1.4 $\pm$ 0.1. By the same principles as for the Mg solution, the phase diagram, solubility, and average molal concentration at the moment of nucleation are derived for the Fe solution (Y=0.12) and presented in Fig 4.7C (See supplementary for determination of $< C(t_n) >$). In the microcapillaries with evaporating Fe solution an extremely high supersaturation is

reached of $< S >_{Fe} = < C(t_n) > / C^*_{III}$ = 3.0 $\pm$ 0.2 at RH=40%. Desarnaud et al. consistently observed elevated supersaturation levels at the onset of sodium chloride crystal nucleation within microcapillaries, regardless of variations in size, shape, and surface properties of the microcapillaries [19]. While achieving high supersaturation in microcapillaries is a more general observed phenomenon, the reported supersaturation levels prior to this study (S $\sim$ 1.6) are still approximately a factor 2 lower than what we observed in our experiments with the Fe solution.

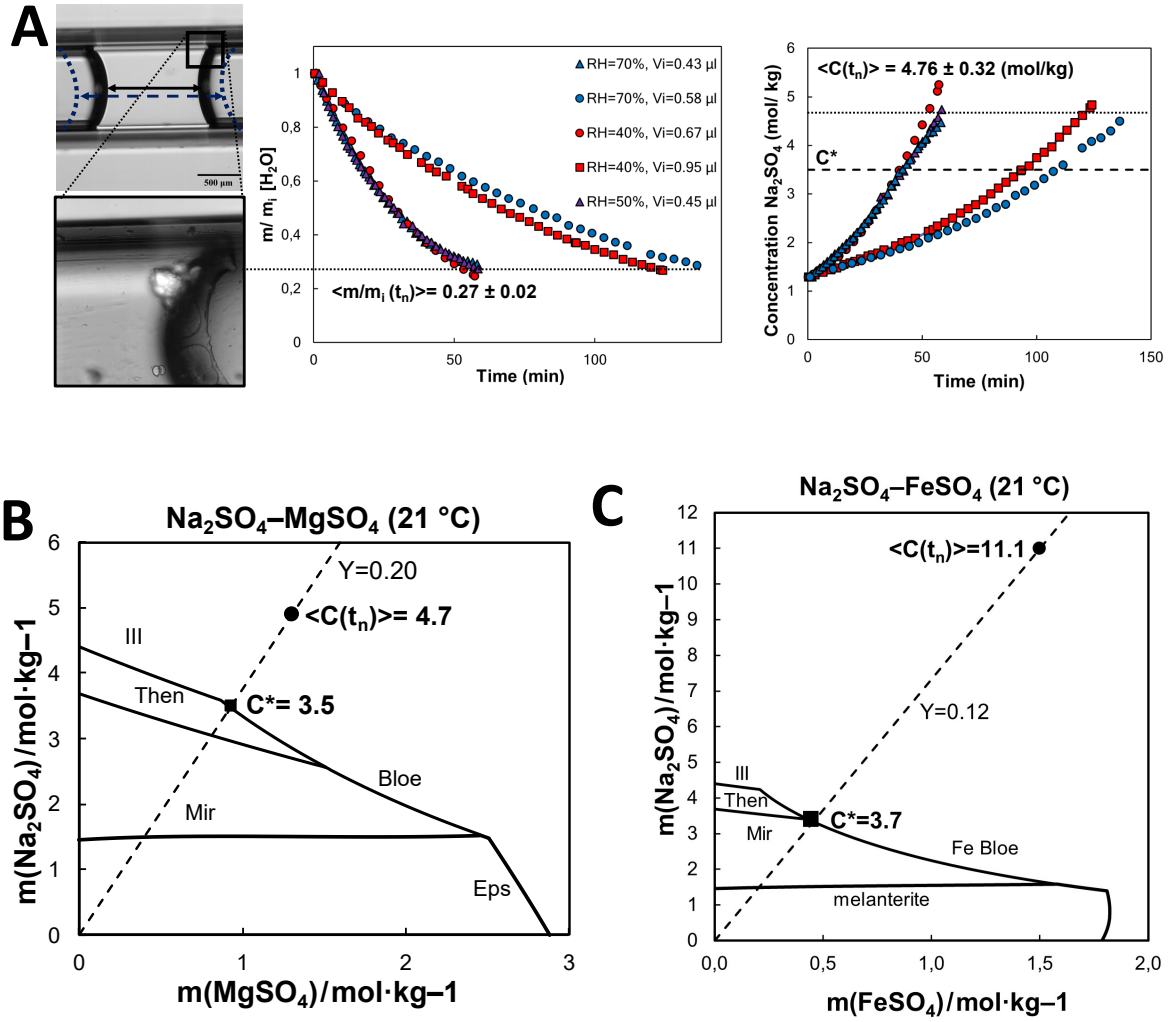

Figure 4.7: **Determination of supersaturation by evaporation in microcapillaries** (**A**) Increasing concentration of dissolved Na_2SO_4 during evaporation (right) in Y_{Mg} = 0.2 solution determined from the fraction of remaining solution m/m_i (left). **(B,C)** Phase diagrams of the two salt mixtures at (21 °C); (**B**) $Na_2SO_4 - MgSO_4$, the average supersaturation $< S >_{Mg} = < C(t_n) > / C^*_{III}$ = 1.4 $\pm$ 0.1 (**C**) $Na_2SO_4 - FeSO_4$, the average supersaturation $< S >_{Fe}$=3.0 $\pm$ 0.2.

4.8. Indirect viscosity measurements, as a function of the supersaturation

Our previous findings elucidate how adding ions induces the formation of a gel network that competes with the crystallization process. As mentioned before, the conclusion of Magill and others that an increased viscosity is required for spherulitic growth is agreed upon by many but not by all [48]. For certain case-by-case studies that report the growth of spherulites, an increased viscosity seems unlikely. However, the actual quantifications of the conditions are often missing. Spherulitic growth in salt solutions is such an example in which a significant increase in viscosity is not directly suspected. In this experiment, the viscosity of the salt solution before spherulites formation is measured with a rheometer by preparing the initial Mg solution that is used to study the growth of spherulites ($Y_{Mg} = 0.2$) with a

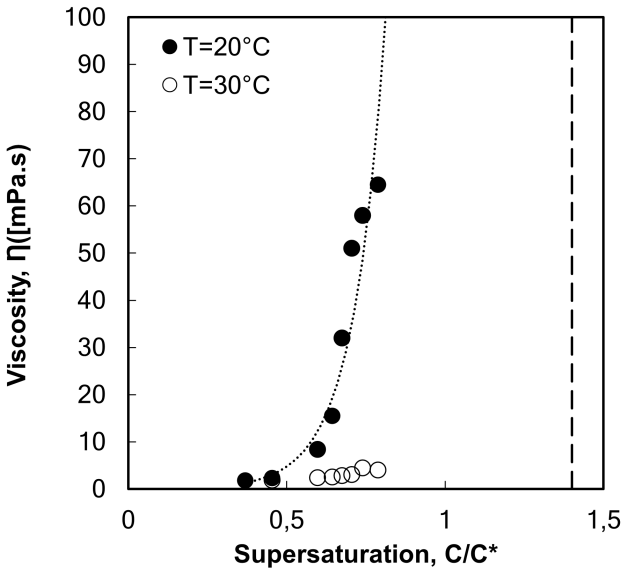

Figure 4.8: **Viscosity as a function of the supersaturation** The exponential fit of T= 20 °C (dotted line) is $\eta = 0.036e^{9.76*S}$ ($R^2 = 0.88$). The viscosity is measured until S=0.79; by then, it has already increased to 64.5 * η_{H_2O}. From the exponential fit, it is suspected that the viscosity can reach up to ~ 30 Pa·s before spherulitic growth is initiated at $S_{Y_{Mg}=0.2} = C/C^* = 1.4$ (dashed line).

reduced mass of water compared to the initial mass of water. The solutions with a reduced amount of water correspond to further stages of evaporation by which water is removed from the evaporating droplets in previous experiments. The stages of evaporation can be defined by the water loss, $(m_i - m)/m_i$. To ensure that the salt solutions are completely dissolved, the solutions are heated to 30 °C under the rheometer by a Peltier element. The temperature is brought back to T=20°C, and the viscosity is measured with a continuous shear rate of 900 $s^{-}1$ and a cone-plate geometry. As determined before, the spherulites nucleate when $(m_i - m)/m_i$= 0.73, which corresponds to a supersaturation of 1.4. In this experiment, we were limited by the ability to dissolve the solutions at higher concentrations completely. Therefore, the viscosity is measured up until S=0.79 ($(m_i - m)/m_i$ = 0.53). The results are presented in Fig.4.8 and show that the viscosity exponentially increases with the supersaturation (dotted line). The dashed line indicates the supersaturation that is reached when the spherulites nucleate (S=1.4). At a supersaturation of 0.79, we measure that the viscosity is already 64.5 times the viscosity of water. If the viscosity follows the exponential trend, the viscosity increases to 30.9 Pa·s when the spherulites nucleate (S=1.4). Interestingly, our results agree with the critically large viscosity reported by Magill for spherulitic growth, typically falling within the range of 30-50 Pa·s[48].

We successfully quantified the viscosity increase preceding spherulitic crystallization. The observed viscosity rise can be attributed to a sol-gel transition since attaining a glassy state would require a viscosity surpassing 10^5 Pa.s. Consequently, this sol-gel transition reduces the diffusion rate, elucidating the diffusive-limited growth mechanism by which we found the spherulites to grow. If we look more closely at the SEM image in Fig.4.2(A), we observe another solid phase between the spherulites that should be the gel residue after complete dehydration.

4.9. Raman identification of the gel state

So far, we have investigated the growth of the spherulites, which we know to consist of pure sodium sulfate phase III. However, what happens to the bivalent ions and how they induce gel formation is still unclear. Interestingly, the bivalent ions (Mg^{2+} and Fe^{2+}) are metal ions that can undergo a sol-gel transition through hydrolysis and condensation [13]. Therefore, we suspect the bivalent ions to be involved in the gel formation. To quantify this hypothesis, we performed two experiments with Raman Spectroscopy.

In the first experiment (Fig. 2(A)), we measured the Raman shift on three locations in a Y_{Mg}= 0.66

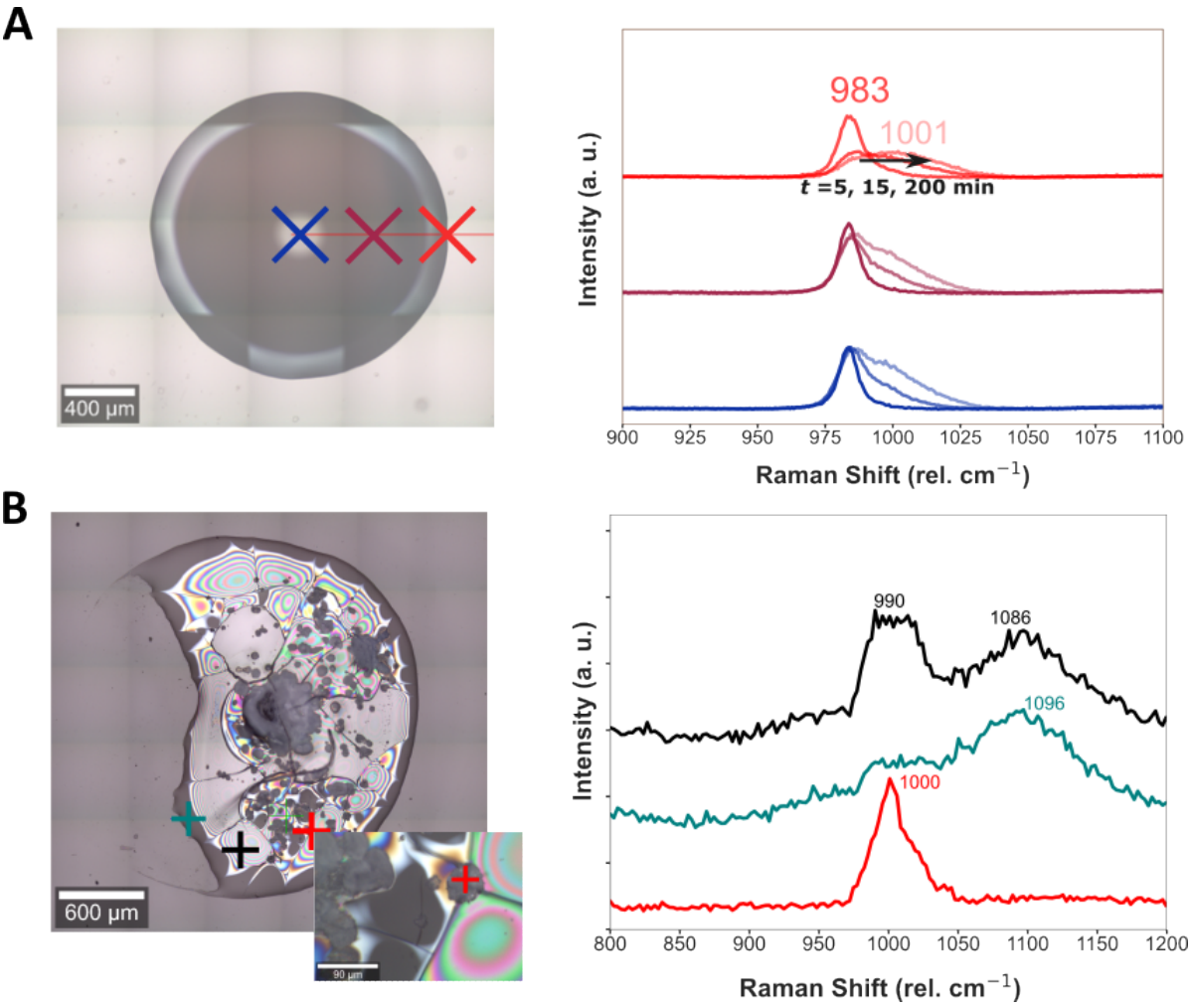

Figure 4.9: **Raman identification of the gel state** (**A**) Raman spectra of three locations in a $Y_{Mg} = 0.66$ droplet after 5, 15 and 200 minutes of evaporation, showing a shift and widening of the ν_1 peak of sulfate. (**B**) A droplet of the gel state at $Y_{Mg} = 0.5$ shows birefringence and spherulites after 18 days of drying.

droplet after 5, 15, and 200 minutes of evaporation. All locations have a wide peak at 983 cm^{-1} after 5 minutes corresponding to the first vibrational mode of Epsomite ($MgSO_4 \cdot 7H_2O$)[82]. This peak is significantly wider after 15 and 200 minutes, indicating a structural distortion or amorphization [82] that we would expect from the sol-gel transition. On the edge of the droplet, the 983 peak is shifted to a wide bump between 975-1025 cm^{-1} that is centred at 1001 cm^{-1}, while in the bulk, the peak instead evolved as a shoulder. The shift happens faster at the edge of the droplet due to the higher evaporation at the three-phase contact line. The Raman spectra of the hydrated phases and anhydrous phase of magnesium sulfates have been reported by Wang et al. (2006)[82], of which the amorphous phases are believed to be most abundantly present on Mars. Interestingly, a comparison between the Raman spectra of the hydrated magnesium sulfate phases reveals a noticeable rightward shift in the ν_1 peak, indicating a reduction in the degree of hydration. Therefore, we can assign the transition in the first hour(s) of drying to the dehydration of an amorphous hydrated state of magnesium sulfate. Interestingly, if we compare our data to that of Wang et al. (2006) [82], we find the peak at 1001 cm^{-1} to correspond to Starkeyite ($MgSO_4 \cdot 4H_2O$) that has a peak at 1000.3 cm^{-1}. Moreover, Wang et al.[82] report the evidence (XRD) of an amorphous phase of Sanderite ($MgSO_4 \cdot 2H_2O$). However, our findings suggest that an amorphous phase of Starkeyite might also form upon dehydration.

In the second experiment (Fig 2.(B)), we measure Raman shifts in a droplet that contains spherulites as well as large areas of the amorphous state ($Y_{Mg} = 0.5$) after 18 days of drying. On the edge, where we only observe the amorphous state (ocean green point), the Raman shift still has a bit of a bump around the 1000 cm^{-1}. More prominent is the disordered region centred at 1096. Sulfate peaks around

1100 cm^{-1} are attributed to the third basic vibrational mode of SO_4 tetrahedra, which corresponds to the asymmetric S-O stretch [43]. Based on the transition from the first vibrational mode to a wide third vibrational mode, we suspect, based on the wide asymmetric S-O peak, that SO_4 tetrahedra formed an ionic glass network upon complete dehydration of the gel, with Mg^{2+} glass modifiers that are located between the network. As described in the study of Calahoo and Wondraczek [15], Mg^{2+} is known to be a high field cation that can work both as a modifier and intermediate in the formation of glass, depending on their local environment [15]. Moreover, ${SO_4}^{2-}$ is an oxoanion that can form an ionic glass in the presence of a significant amount of conventional glass modifier (Mg^{2+}, Na^{+}, K^{+}). The black peak is the Raman measurement of a location in the amorphous area that is further from the edge. Here, we see a bump in both areas of the Raman spectrum that can correspond to a transition or coexistence between the gel and glass-like networks.

In short, we observe a transition in the Raman shift in areas where the gel state is predominant. Based on our observations and the work of Wang et al.[82], we suspect the sol-gel transition to involve a disorganized phase of one or more hydrated magnesium sulfate(s). When the gel state further dehydrates, the sulfate can form a tetrahedral glass network in the presence of the bivalent ions that work as glass modifiers. At the edge of the droplet where the water evaporates at a higher rate, the transition induced by dehydration is further evolved. Similarly to Mg^{2+}, the Fe^{2+} cations could also work as a network modifier. However, the Raman spectra presented here and their interpretation are all preliminary results that will be further investigated by continuous research in our group on sol-gel transition from evaporative salt mixtures.

5

Discussion

We explored the initiation and growth processes leading to the formation of Na_2SO_4 spherulites in evaporating salt mixtures. During evaporation, sodium sulfate from a pure solution typically evolves into regular polyhedral crystals. However, in silica-free sulfate mixtures, a sol-gel transition precedes spherulitic growth. Notably, this sol-gel transition is induced by the addition of bivalent (metal) ions, such as Fe^{2+} or Mg^{2+}. While metal ions have been recognized to induce a sol-gel transition through condensation [13], our study uniquely demonstrates its utility in controlling the morphological development of crystals in evaporating salt solutions.

The bivalent-containing sulfate salt mixtures that are studied here exhibit spherulitic growth of the metastable phase III of sodium sulfate. Utilizing the Pitzer model by Steiger et al. [69], we determined the thermodynamic properties of sodium sulfate phases in the binary salt systems $Na_2SO_4 - FeSO_4$ and $Na_2SO_4 - MgSO_4$. Based on the solubility of Phase III in these binary salt mixtures, we found that the systems are saturated far beyond the solubilities of Phase III when the spherulitic growth is initiated, with supersaturations of 1.4 $\pm$ 0.1 in the Mg solution and 3.0 $\pm$ 0.2 in the Fe solution. Moreover, our results show how the spherulitic crystals evolve. The morphological evolution can be separated into three stages: (1) formation of microsized pre-nucleation clusters, (2) growth of premature spherulites to fully developed (round) spherulites, and (3) evolution to stable forms. We observed that a smooth crystal can undergo spherulitic growth before attaining its final morphology. Therefore, we can attribute spherulitic morphologies to the metastable zone, which can evolve into other shapes as the supersaturation decreases.

We have demonstrated that the final spherulitic morphology can be controlled by adjusting the molar fraction of bivalent ions, the evaporation rate, or inducing geometric constraints. We identified the range of molal fractions conducive to spherulitic growth to be $0.03 < Y_{Fe} < 0.29$ and $0.18 < Y_{Mg} < 0.46$ in sodium sulfate solutions. The spherulitic sodium sulfate crystals are formed by a diffusive growth mechanism in both sulfate mixtures, where L (μm) $\sim \Delta\sqrt{t}$, with $3.9 \leq \Delta \leq 9.6$. The interplay between the diffusion rate (D), influenced by viscosity, and the rate of integration (G) that depends on supersaturation determines the growth mechanism. The sol-gel transition causes supersaturation to reach extremely high values before spherulite nucleation, making diffusion the limiting factor for growth. However, in the bulk of an evaporating droplet with more solvent available, the growth rate (G) converges towards the diffusion rate (D) due to ion consumption by spherulitic growth. This principle explains why a transition from spherulitic growth to other growth modes can be avoided by increasing the evaporation rate, enhancing the sol-gel transition by adding more bivalent ions or introducing geometrical constraints to limit solvent availability.

Finally, we studied how the sol-gel transition leads to an increased viscosity that delays nucleation and inhibits rapid growth. The viscosity in the Mg solution was found to increase exponentially with supersaturation, reaching approximately 30 Pa·s at the initiation of spherulitic growth, falling in the range of the previously reported required viscosity for spherulitic growth by Magill et al. [48]. Preliminary results with Raman Spectroscopy suggest that the sol-gel transition involves amorphization of one or more hydrated magnesium sulfate(s) by dehydration. Further dehydration of the gel may lead to sulfate forming a tetrahedral glass network in the presence of bivalent ions as glass modifiers. However, the spontaneous formation of a gel or glass at room temperature from a salt solution is a very interesting

study in itself and requires further investigation.

In conclusion, our findings provide insights into growing (sulfate) salts into perfectly developed spherulites, offering potential applications in various industrial crystallization processes. Moreover, understanding the growth mechanisms and controlling parameters expands our knowledge of crystallization conditions that facilitate the magnificent self-assembly of nanocrystals that form spherulites.

6

Conclusions and recommendations

We have successfully addressed the research objectives outlined in the introduction. Specifically, our findings establish that bivalent ions induce a sol-gel transition in sulfate salt mixtures, offering a versatile means to modulate growth conditions in such systems. Furthermore, quantification of the growth conditions at the initiation of spherulitic growth revealed two critical factors: an increase in viscosity on the order of 30 Pa·s, which retards the nucleation and growth, and a high supersaturation level so that the concentration reaches far above the metastable needle-shaped crystal phase. Furthermore, we found that the pivotal experimental parameters to control the growth and morphology of precipitating spherulites are the molal fraction of bivalent ions in the sulfate mixture, the evaporation rate, and geometrical constraints. Notably, our study unveils that spherulitic crystal growth is diffusion-limited. Viscosity emerges as a key factor in triggering diffusive-limited growth mechanisms. While this phenomenon was anticipated for polymeric spherulites, our study establishes its occurrence in evaporative salt solutions at room temperature.

For enhanced control, future investigations should delve into understanding how metal ions induce a sol-gel transition during the evaporation of salt mixtures at room temperature. Furthermore, the observed pre-nucleation clusters suggest a potential two-step nucleation process, a hypothesis that awaits validation in subsequent research. Last but not least, expanding the scope of experiments to include salts beyond sulfates would be beneficial, exploring whether bivalent ions induce spherulitic growth in a manner analogous to our findings in this study. This comparative analysis could provide valuable insights into the generalizability of our observed phenomena across different salt systems.

7

Appendix

7.1. Appendix

7.1.1. Characteristics of ions

The ionic properties of the cations that are present in the sulfate mixtures are reported by Nightingale [52] and listed in Table 7.1. The ionic radius of magnesium is slightly smaller in its dehydrated form than of iron. Interestingly, in aqueous solutions, the hydrated radius of Fe^{2+} is the same as the hydrated radius of Mg^{2+}.

Ion	Dehydrated Radius (Å)	Hydrated Radius (Å)
Na^{2+}	0.95	3.58
Fe^{2+}	0.75	4.28
Mg^{2+}	0.65	4.28

Table 7.1: **Dehydrated and hydrated radii of the cations in the sulfate mixtures at T = 25 °C** , from Nightingale [52].

7.1.2. Salt properties

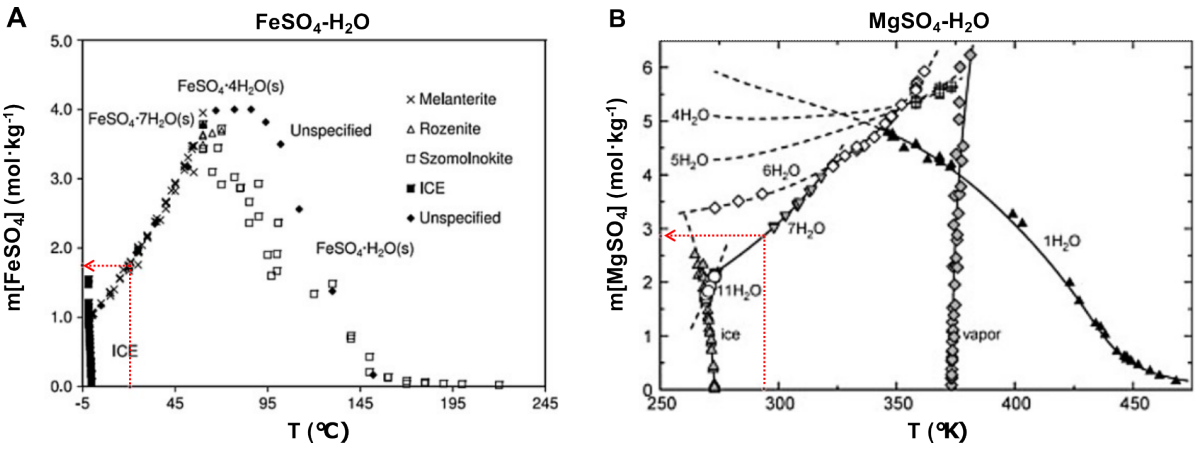

Figure 7.1: **Solubility phase diagrams of the metal sulfate hydrates (A)** $FeSO_4 - H_2O$ phase diagram, reported by Kobylin et al. [37]. **(B)** $MgSO_4 - H_2O$ phase diagram, reported by Steiger et al. [70]. Determination of solubility at experimental conditions (T=20.5 $\pm$ 1 °C) is illustrated by red dotted arrows. The solubility of iron sulfate (heptahydrate) is 1.75 $\pm$ 0.03 mol.kg^{-1} and of magnesium sulfate (heptahydrate) is 2.86 $\pm$ 0.03 mol.kg^{-1}.

The thermodynamic properties of the salts that are dissolved in the two sulfate mixtures of this study, are summarized in this section. The solubilities in water at the experimental conditions are determined from the phase diagrams that are reported in literature by Kobylin et al. [37] and Steiger et al. [70]. The

solubility phase diagram of sodium sulfate is presented in Fig. 4.1(A). The solubility phase diagrams of iron sulfate and magnesium sulfate are given in Fig. 7.1. Together with their molar mass, we have summarized the solubilities at the experimental conditions (T=20.5 $\pm$ 1 °C) all compounds in Table 7.2.

Compound	Molar Mass (g/mol)	Solubility in water (mol.kg^{-1})
Sodium Sulfate (Na_2SO_4) V	142.04	3.69 $\pm$ 0.02
Sodium Sulfate (Na_2SO_4) III	142.04	4.42 $\pm$ 0.02
Sodium Sulfate Decahydrate ($Na_2SO_4 \cdot 10H_2O$)	322.19	1.42 $\pm$ 0.08
Iron(II) Sulfate Heptahydrate ($FeSO_4 \cdot 7H_2O$)	278.01	1.75 $\pm$ 0.03
Magnesium Sulfate Heptahydrate ($MgSO_4 \cdot 7H_2O$)	246.47	2.86 $\pm$ 0.03

Table 7.2: **Molar masses and solubilities in water of sulfate compounds at T = 20.5 $\pm$ 1 °C**

7.1.3. Growth rate of spherulites in iron-sodium sulfate solution

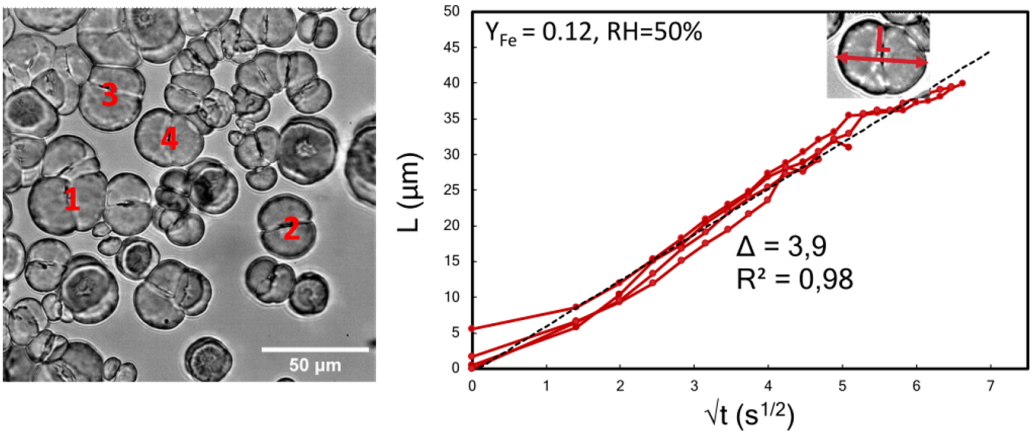

Figure 7.2: **The growth rate of spherulites of Na_2SO_4 at RH=50% in the Fe solution** Measured spherulites are indicated with the numbers 1,2,3 and 4.The length L, of the spherulites is plotted as a function of the square root of time. The linear trend indicates that the growth of the spherulites is controlled by diffusion.

7.1.4. Determination of supersaturation in iron-sodium sulfate solution

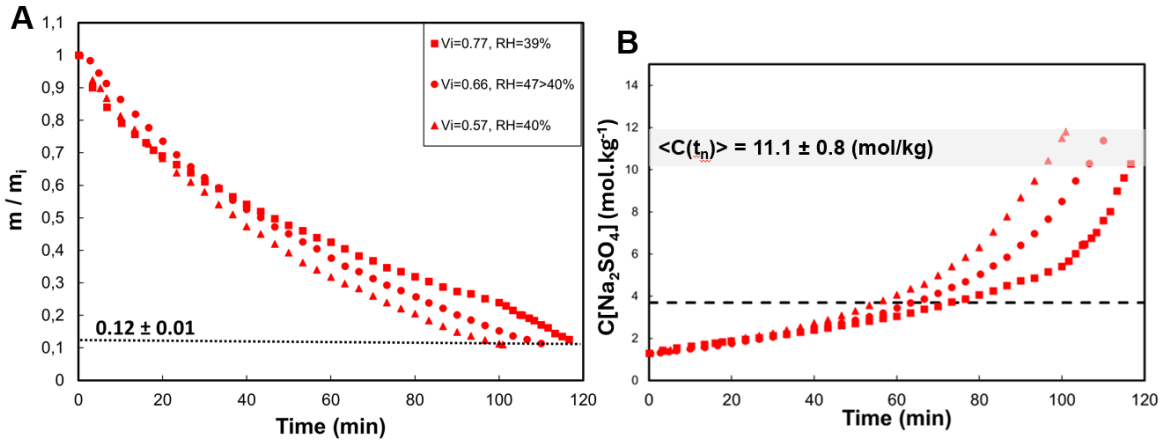

Figure 7.3: **Determination of supersaturation by evaporation of Fe solution in microcapillaries** (**A**) Increasing concentration of dissolved Na_2SO_4 during evaporation (right) in $Y_{Fe} = 0.12$ solution determined from the fraction of remaining solution m/m_i (left). The average supersaturation $< S >_{Fe} = < C(t_n) > / C^*_{III}$ = 3.0 $\pm$ 0.2.

Bibliography

[1] MI Abo el Maaty, IL Hosier, and DC Bassett. “A unified context for spherulitic growth in polymers”. In: *Macromolecules* 31.1 (1998), pp. 153–157.

[2] Saghir Akhtar, Cofin W Pouton, and Lidia J Notarianni. “The influence of crystalline morphology and copolymer composition on drug release from solution cast and melt-processed P (HB-HV) copolymer matrices”. In: *Journal of controlled release* 17.3 (1991), pp. 225–233.

[3] Jens-Petter Andreassen and Alison Emslie Lewis. “Classical and nonclassical theories of crystal growth”. In: *New Perspectives on Mineral Nucleation and Growth: From Solution Precursors to Solid Materials* (2017), pp. 137–154.

[4] MI Artsis et al. “Biodegradation and medical application of microbial poly (3-hydroxybutyrate)”. In: *Molecular Crystals and Liquid Crystals* 523.1 (2010), pp. 21–593.

[5] Usama Al-Atar et al. “Mechanism of calcium oxalate monohydrate kidney stones formation: layered spherulitic growth”. In: *Chemistry of Materials* 22.4 (2010), pp. 1318–1329.

[6] David Clifford Bassett. “On spherulitic growth and cellulation in polymers. A Unified Context”. In: *Polymer journal* 31.9 (1999), pp. 759–764.

[7] DC Bassett. “Polymer spherulites: a modern assessment”. In: *Journal of Macromolecular Science, Part B* 42.2 (2003), pp. 227–256.

[8] J Bisault, G Ryschenkow, and Gabriel Faivre. “Spherulitic branching in the crystallization of liquid selenium”. In: *Journal of crystal growth* 110.4 (1991), pp. 889–909.

[9] Michael A Boles et al. “The surface science of nanocrystals”. In: *Nature materials* 15.2 (2016), pp. 141–153.

[10] Daniel Bonn and Noushine Shahidzadeh. “Multistep crystallization processes: How not to make perfect single crystals”. In: *Proceedings of the National Academy of Sciences* 113.48 (2016), pp. 13551–13553.

[11] Christoph Breitkreuz, Jens Götze, and Alexandra Weißmantel. “Mineralogical and geochemical investigation of megaspherulites from Argentina, Germany, and the USA”. In: *Bulletin of Volcanology* 83 (2021), pp. 1–24.

[12] David Brewster. “XLIII.—On Circular Crystals”. In: *Earth and Environmental Science Transactions of The Royal Society of Edinburgh* 20.4 (1853), pp. 607–623.

[13] C Jeffrey Brinker and George W Scherer. *Sol-gel science: the physics and chemistry of sol-gel processing*. Academic press, 2013, pp. 21–58.

[14] Fabian Burkhardt. “The Crystal Structure of the New Ternary Al8Cr4Sc Phase in the Al-Cr-Sc Push-Pull Alloy”. PhD thesis. Apr. 2018.

[15] Courtney Calahoo and Lothar Wondraczek. “Ionic glasses: Structure, properties and classification”. In: *Journal of Non-Crystalline Solids: X* 8 (2020), p. 100054.

[16] Buckley Crist and Jerold M Schultz. “Polymer spherulites: A critical review”. In: *Progress in Polymer Science* 56 (2016), pp. 1–63.

[17] Preshit Dandekar, Zubin B Kuvadia, and Michael F Doherty. “Engineering crystal morphology”. In: *Annual Review of Materials Research* 43 (2013), pp. 359–386.

[18] Robert Darkins et al. “Calcite kinetics for spiral growth and two-dimensional nucleation”. In: *Crystal Growth & Design* 22.7 (2022), pp. 4431–4436.

[19] Julie Desarnaud et al. “Hopper growth of salt crystals”. In: *The journal of physical chemistry letters* 9.11 (2018), pp. 2961–2966.

[20] MI Abo El Maaty and DC Bassett. “On fold surface ordering and re-ordering during the crystallization of polyethylene from the melt”. In: *Polymer* 42.11 (2001), pp. 4957–4963.

[21] Paul Flowers et al. *10.4 phase diagrams*. en. https://openstax.org/books/chemistry-2e/pages/10-4-phase-diagrams. Accessed: 2024-1-1.

[22] AD Fowler et al. “Supercooled rocks: development and significance of varioles, spherulites, dendrites and spinifex in Archaean volcanic rocks, Abitibi Greenstone belt, Canada”. In: *Precambrian Research* 115.1-4 (2002), pp. 311–328.

[23] Alexy P Freitas et al. “Crystallization within Intermediate Amorphous Phases Determines the Polycrystallinity of Nanoparticles from Coprecipitation”. In: *Nano Letters* 22.1 (2021), pp. 29–35.

[24] Helmut Goesmann and Claus Feldmann. “Cover Picture: Nanoparticulate Functional Materials (Angew. Chem. Int. Ed. 8/2010)”. In: *Angewandte Chemie International Edition* 49.8 (2010), pp. 1362–1395.

[25] Nigel Goldenfeld. “Theory of spherulitic crystallization”. In: *Journal of crystal growth* 84.4 (1987), pp. 601–608.

[26] Monojoy Goswami et al. “Understanding supercooling mechanism in sodium sulfate decahydrate phase-change material”. In: *Journal of Applied Physics* 129.24 (2021).

[27] Laszlo Granasy et al. “Growth of’dizzy dendrites’ in a random field of foreign particles”. In: *Nature Materials* 2.2 (2003), pp. 92–96.

[28] László Gránásy et al. “Growth and form of spherulites”. In: *Physical Review E* 72.1 (2005), p. 011605.

[29] László Gránásy et al. “Phase-field modeling of polycrystalline solidification: from needle crystals to spherulites—a review”. In: *Metallurgical and Materials Transactions A* 45 (2014), pp. 1694–1719.

[30] Daniel Griffin et al. “Supersaturation Control during Fractional Crystallization”. In: Sept. 2014.

[31] Maurits CR Heijna et al. “Spherulitic growth of hen egg-white lysozyme crystals”. In: *The Journal of Physical Chemistry B* 111.7 (2007), pp. 1567–1573.

[32] Lee-Way Jin et al. “Imaging linear birefringence and dichroism in cerebral amyloid pathologies”. In: *Proceedings of the National Academy of Sciences* 100.26 (2003), pp. 15294–15298.

[33] Taesung Jung, Woo-Sik Kim, and Chang Kyun Choi. “Crystal structure and morphology control of calcium oxalate using biopolymeric additives in crystallization”. In: *Journal of crystal growth* 279.1-2 (2005), pp. 154–162.

[34] HD Keith and FJ Padden Jr. “A phenomenological theory of spherulitic crystallization”. In: *Journal of Applied Physics* 34.8 (1963), pp. 2409–2421.

[35] A Keller. “Investigations on banded spherulites”. In: *Journal of Polymer Science* 39.135 (1959), pp. 151–173.

[36] R James Kirkpatrick. “Kinetics of crystal growth in the system CaMgSi 2 O 6-CaAl 2 SiO 6”. In: *American Journal of Science* 274.3 (1974), pp. 215–242.

[37] PM Kobylin, Hannu Sippola, and PA Taskinen. “Thermodynamic modelling of aqueous Fe (II) sulfate solutions”. In: *Calphad* 35.4 (2011), pp. 499–511.

[38] Uwe Köster and Petra Weiss. “Crystallization and decomposition of amorphous silicon-aluminium films”. In: *Journal of Non-Crystalline Solids* 17.3 (1975), pp. 359–368.

[39] Mark RH Krebs et al. “The formation of spherulites by amyloid fibrils of bovine insulin”. In: *Proceedings of the National Academy of Sciences* 101.40 (2004), pp. 14420–14424.

[40] Mark Ladd. *The essence of crystallography*. World Scientific, 2019.

[41] JS Langer. “Dynamics of dendritic pattern formation”. In: *Materials science and engineering* 65.1 (1984), pp. 37–44.

[42] DD Le Pevelen. “8.4 Physical Separations: Solid-State Forms and Habits of Chiral Substances”. In: (2012).

[43] M Lenoir et al. “Quantitation of sulfate solubility in borosilicate glasses using Raman spectroscopy”. In: *Journal of Non-Crystalline Solids* 355.28-30 (2009), pp. 1468–1473.

[44] Shankun Liang et al. “Supersaturation-driven self-assembly formation of ceftriaxone sodium spherulites: From amorphous form to spherulites”. In: *Particuology* 90 (2024), pp. 10–19. ISSN: 1674-2001.

[45] Matthew T Lloyd et al. “Efficient solution-processed photovoltaic cells based on an anthradithiophene/fullerene blend”. In: *Journal of the American Chemical Society* 129.29 (2007), pp. 9144–9149.

[46] Ursula V Lay Ma, John D Floros, and Gregory R Ziegler. “Formation of inclusion complexes of starch with fatty acid esters of bioactive compounds”. In: *Carbohydrate polymers* 83.4 (2011), pp. 1869–1878.

[47] Elena Macías-Sánchez et al. “Spherulitic crystal growth drives mineral deposition patterns in collagen-based materials”. In: *Advanced Functional Materials* 32.31 (2022), p. 2200504.

[48] JH Magill. “Review spherulites: A personal perspective”. In: *Journal of materials science* 36 (2001), pp. 3143–3164.

[49] Ryan Molecke. *Surface Extrapolation by Reverse-Plotting of Energy Trajectories*. `http://www.unm.edu/~reason/SERPEnT_intro.html`. [Accessed 10-10-2023].

[50] Harry Wheeler Morse, Charles Hyde Warren, and JDH Donnay. “Artificial spherulites and related aggregates”. In: *American Journal of Science* 5.137 (1932), pp. 421–439.

[51] William W Mullins and RF Sekerka. “Stability of a planar interface during solidification of a dilute binary alloy”. In: *Journal of applied physics* 35.2 (1964), pp. 444–451.

[52] ER Nightingale Jr. “Phenomenological theory of ion solvation. Effective radii of hydrated ions”. In: *The Journal of Physical Chemistry* 63.9 (1959), pp. 1381–1387.

[53] Xiaoqin Ou, Jilt Sietsma, and Maria J Santofimia. “Fundamental study of nonclassical nucleation mechanisms in iron”. In: *Acta Materialia* 226 (2022), p. 117655.

[54] Sione Paea. “Kinetic Monte Carlo (KMC) Algorithm for Nanocrystals”. In: 2011.

[55] D. Patel and D.C. Basset. “On spherulitic crystallization and the morphology of melt-crystallized poly(4-methylpentene-1)”. In: *Proceedings of the Royal Society of London. Series A: Mathematical and Physical Sciences* 445.1925 (1994), pp. 577–595.

[56] Kenneth S Pitzer. “Ion interaction approach: theory and data correlation”. In: *Activity coefficients in electrolyte solutions*. CRC Press, 2018, pp. 75–153.

[57] Siddharth Rath. “Comparison of CPFEM and spectral solution methods in prediction of strains near grain boundaries in a uniaxially loaded oligocrystalline tensile specimen”. PhD thesis. Aug. 2016, p. 6.

[58] G Ryschenkow and G Faivre. “Bulk crystallization of liquid selenium Primary nucleation, growth kinetics and modes of crystallization”. In: *Journal of crystal growth* 87.2-3 (1988), pp. 221–235.

[59] Bram Sadlik. “The role of viscosity in banded-spherulitic growth”. In: (2004).

[60] Manon Schindler. “Deracemization of Sodium Chlorate with or without the Influence of Sodium Dithionate”. PhD thesis. Normandie Université, 2020.

[61] Robert F Sekerka. “Theory of crystal growth morphology”. In: *Crystal Growth-From Fundamentals to Technology*. Elsevier, 2004, pp. 55–93.

[62] Noushine Shahidzadeh and Julie Desarnaud. “Damage in porous media: role of the kinetics of salt (re) crystallization”. In: *The European Physical Journal-Applied Physics* 60.2 (2012), p. 24205.

[63] S Shakiba et al. “Time scale based analysis of in-situ crystal formation in droplet undergoing rapid dehydration”. In: *International Journal of Pharmaceutics* 560 (2019), pp. 47–56.

[64] Jialiang Shi, Michael C Sweedman, and Yong-Cheng Shi. “Structure, birefringence and digestibility of spherulites produced from debranched waxy maize starch”. In: *International Journal of Biological Macromolecules* 183 (2021), pp. 1486–1494.

[65] Alexander G Shtukenberg et al. “Spherulites”. In: *Chemical reviews* 112.3 (2012), pp. 1805–1838.

[66] Jacek Siódmiak and Adam Gadomski. “Spherulites: How Do They Emerge at an Onset of Nonequilibrium Kinetic-Thermodynamic and Structural Singularity Addressing Conditions?” In: *Entropy* 24.5 (2022), p. 663.

[67] Ella Sokol et al. “CaC2O4· H2O spherulites in human kidney stones: morphology, chemical composition, and growth regime”. In: *European Journal of Mineralogy* 17.2 (2005), pp. 285–295.

[68] Michael Steiger and Sönke Asmussen. “Crystallization of sodium sulfate phases in porous materials: The phase diagram Na2SO4–H2O and the generation of stress”. In: *Geochimica et Cosmochimica Acta* 72.17 (2008), pp. 4291–4306.

[69] Michael Steiger, Jana Kiekbusch, and Andreas Nicolai. “An improved model incorporating Pitzer’s equations for calculation of thermodynamic properties of pore solutions implemented into an efficient program code”. In: *Construction and Building Materials* 22.8 (2008), pp. 1841–1850.

[70] Michael Steiger et al. “Decomposition reactions of magnesium sulfate hydrates and phase equilibria in the MgSO4–H2O and Na+–Mg2+–Cl—SO42—H2O systems with implications for Mars”. In: *Geochimica et Cosmochimica Acta* 75.12 (2011), pp. 3600–3626.

[71] Ichiro Sunagawa. *Crystals: growth, morphology, & perfection*. Cambridge University Press, 2007.

[72] Ichiro Sunagawa. “Growth and morphology of diamond crystals under stable and metastable contitions”. In: *Journal of Crystal Growth* 99.1, Part 2 (1990), pp. 1156–1161. ISSN: 0022-0248.

[73] Ichiro Sunagawa. “Growth histories of mineral crystals as seen from their morphological features”. In: *Crystal Growth Technology*. Elsevier, 2003, pp. 1–23.

[74] William Henry Fox Talbot. “IV. Further observations on the optical phenomena of crystals”. In: *Philosophical Transactions of the Royal Society of London* 127 (1837), p. 25.

[75] Vladimir L Tassev and Shivashankar R Vangala. “Thick hydride vapor phase heteroepitaxy: a novel approach to growth of nonlinear optical materials”. In: *Crystals* 9.8 (2019), p. 393.

[76] Amit K Thakur et al. “A critical review on thermodynamic and hydrodynamic modeling and simulation of liquid antisolvent crystallization of pharmaceutical compounds”. In: *Journal of Molecular Liquids* 362 (2022), p. 119663.

[77] William A Tiller. *The science of crystallization: macroscopic phenomena and defect generation*. Cambridge University Press, 1991.

[78] A Toda. “Spherulitic growth in crystalline polymers”. In: *Encyclopedia of polymers and composites* (2013), pp. 1–12.

[79] Alexander Toifl. “Numerical methods for three-dimensional selective epitaxy and anisotropic wet Etching simulations”. PhD thesis. Wien, 2021.

[80] Richard Tran et al. “Surface energies of elemental crystals”. In: *Scientific data* 3.1 (2016), pp. 1–13.

[81] Osamu Urakawa et al. “Self-diffusion and viscosity of low molecular weight polystyrene over a wide temperature range”. In: *Macromolecules* 37.4 (2004), pp. 1558–1564.

[82] Alian Wang et al. “Sulfates on Mars: A systematic Raman spectroscopic study of hydration states of magnesium sulfates”. In: *Geochimica et cosmochimica acta* 70.24 (2006), pp. 6118–6135.

[83] Yun-Wei Wang, Hugo K Christenson, and Fiona C Meldrum. “Confinement leads to control over calcium sulfate polymorph”. In: *Advanced Functional Materials* 23.45 (2013), pp. 5615–5623.

[84] JS Wettlaufer, Martin Jackson, and M Elbaum. “A geometric model for anisotropic crystal growth”. In: *Journal of Physics A: Mathematical and General* 27.17 (1994), p. 5957.

[85] Rozeline Wijnhorst et al. “Softness of hydrated salt crystals under deliquescence”. In: *Nat. Commun.* 14.1 (2023), p. 1090.

[86] Wikipedia. *Surface-area-to-volume ratio*. `https://en.wikipedia.org/wiki/Surface-area-to-volume_ratio`. [Accessed 21-Jul-2023].

[87] EM Woo and Siti Nurkhamidah. “Surface nanopatterns of two types of banded spherulites in poly (nonamethylene terephthalate) thin films”. In: *The Journal of Physical Chemistry B* 116.16 (2012), pp. 5071–5079.

[88] Yuntian Xiao et al. “Growth mechanism of the spherulitic propylthiouracil–kaempferol cocrystal: new perspectives into surface nucleation”. In: *CrystEngComm* 23.12 (2021), pp. 2367–2375.

[89] G. Zangari. “Fundamentals of Electrodeposition”. In: *Encyclopedia of Interfacial Chemistry*. Ed. by Klaus Wandelt. Oxford: Elsevier, 2018, pp. 141–160.